

1 **A 3D microtumour system that faithfully represents ovarian cancer minimal residual**
2 **disease**

3 Xingyun Yang,^{a†} Mara Artibani,^{b,c†} Yongcheng Jin,^a Aneesh Aggarwal,^{b,c} Yujia Zhang,^a Sandra
4 Muñoz-Galvan,^{b,d} Ellina Mikhailova,^a Lena Rai,^{b,c} Nobina Mukherjee,^a Ravinash Krishna
5 Kumar,^{a,e} Ashwag Albukhari^f, Linna Zhou,^{a,g*} Ahmed Ashour Ahmed,^{b,c*} Hagan Bayley^{a*}

6

7 Affiliation

8 ^aDepartment of Chemistry, University of Oxford, Oxford OX1 3TA, UK

9 ^bOvarian Cancer Cell Laboratory, MRC Weatherall Institute of Molecular Medicine, University of
10 Oxford, Oxford OX3 9DS, UK

11 ^cNuffield Department of Women's & Reproductive Health, University of Oxford, Oxford, OX3 9DU,
12 UK

13 ^dInstituto de Biomedicina de Sevilla, IBiS/Hospital Universitario Virgen del
14 Rocío/CSIC/Universidad de Sevilla, Avda. Manuel Siurot s/n 41013, Seville, Spain

15 ^eCentre for Bioengineering, School of Engineering and Materials Science, Queen Mary University
16 of London, London, E1 4NS, UK

17 ^fBiochemistry Department, Faculty of Science, King Abdulaziz University, Jeddah, Saudi Arabia

18 ^gLudwig Institute for Cancer Research, Nuffield Department of Medicine, University of Oxford,
19 Oxford, OX3 7DQ, UK

20 [†]These authors contributed equally

21 *Correspondence: Linna Zhou (linna.zhou@ludwig.ox.ac.uk), Ahmed Ashour Ahmed
22 (ahmed.ahmed@wrh.ox.ac.uk), Hagan Bayley (hagan.bayley@chem.ox.ac.uk).

24 **Abstract**

25 **Background**

26 Bulk cancer and minimal residual disease (MRD) are characterised by different molecular
27 drivers and therefore necessitate different therapeutic strategies. However, there are currently no
28 3D models that can faithfully recapitulate MRD *ex vivo* for therapy development.

29 **Methods**

30 A microfluidic technique was implemented to construct 3D microtumours, in which tumour cells,
31 either by themselves or with fibroblasts, were encapsulated in viscous hydrogels. The 3D
32 microtumours were analysed for their response to first-line chemotherapeutics and characterised
33 through RNA-Seq, by comparing them to both 2D cultures and clinical samples.

34 **Results**

35 Our microfluidic platform guarantees the fabrication of 3D microtumours of tailorabile size and
36 cell content, which recreate key features of tumours such as hypoxia, characteristic organization of
37 the cytoskeleton and a dose-response to chemotherapeutics close to the physiological range. The
38 3D microtumours were also used to examine non-genetic heterogeneity in ovarian cancer and could
39 fully reflect the recently described “Oxford Classic” five molecular signatures.

40 The gene expression profile of 3D microtumours following chemotherapy treatment closely
41 resembled that of MRD in ovarian cancer patients, showing the upregulation of genes involved in
42 fatty acid metabolism. We demonstrate that these 3D microtumours are ideal for drug development
43 by showing how they support the identification of a promising inhibitor of fatty acid oxidation,
44 perhexiline, which specifically targets chemotherapy-resistant MRD ovarian cancer cells and not
45 bulk cancer cells.

46 **Conclusion**

47 We have obtained the first 3D model of ovarian cancer MRD by using microtumours generated
48 through microfluidics. This system is ideal for high-throughput drug screening and, given its

49 versatility, it can be readily extended to additional types of cancer, as well as accommodate multiple
50 cell types to generate complex tumour microenvironments.

51

52 **Keywords**

53 Minimal residual disease, ovarian cancer, 3D cancer models, microfluidics, high-throughput
54 drug screening platforms

55

56 Background

57 Drug resistance is responsible for up to 90% of cancer-related deaths and can operate through
58 several different mechanisms¹. A particularly challenging group of treatment-resistant cells is
59 represented by Minimal Residual Disease (MRD), the microscopic clusters of malignant cells that
60 remain in patients after complete clinical/radiological response and are capable of reinitiating
61 tumours². Investing in therapeutics that specifically target MRD could help delay or prevent relapses
62 altogether, moving us a step closer to the chronic management or potential eradication of cancer³.

63 However, this long-sought goal has been difficult to achieve, especially in solid tumours:
64 isolating and characterising these cells directly from patients can be quite challenging. Because of
65 this, we lack deep knowledge of MRD biology as well as appropriate experimental models that could
66 be used as screening platforms for effective compounds.

67 One of the few solid tumours where direct characterisation of clinical MRD has been achieved
68 is ovarian cancer⁴. After obtaining the first in-depth transcriptomic characterisation of MRD from
69 patients, we aimed to develop a faithful and physiologically-relevant model of MRD that could be
70 used for drug screening. We considered mouse, 2D and 3D models, all of which have different
71 balances of feasibility, accuracy and cost.

72 Although mouse models exist to study metastatic ovarian cancer, their reproductive physiology⁵
73 as well as omental anatomy (one of the most common MRD sites)⁶ differ from humans and, further,
74 this species does not develop spontaneous ovarian tumours. Conventional 2D cell culture has been
75 a standard *in vitro* model for decades. However, under these conditions, cell morphologies and cell
76 bioactivities deviate from those found *in vivo*⁷. For instance, cells in 2D culture lose diverse
77 phenotypes, have altered cell signalling, rely on different metabolic pathways, and have an unlimited
78 supply of nutrients and oxygen⁸, which means they may not provide biologically meaningful
79 responses to chemotherapeutics. Moreover, a transcriptomic study of single cell-derived spheroids
80 from ovarian cancer ascites has shown that although 2D monolayers support proliferation and
81 tumour growth cascades, 3D spheroids additionally capture aspects of cholesterol and lipid

82 metabolism, which are features of metastatic disease⁹. These pathways are implicated in the lipid
83 signature we observed in ovarian cancer MRD⁴; thus, in this context, 3D models are essential for
84 drug discovery.

85 Another aspect to be considered is that cancers typically organise in 3D, creating a hypoxic
86 setting with intimate intercellular signalling, and ultimately achieve anchorage-independent growth.
87 3D cancer cultures offer extensive cell-cell and cell-ECM (extracellular matrix) interactions¹⁰, and
88 are understood to preserve the cell polarity, morphology, gene expression and topology seen *in*
89 *vivo*^{8, 11, 12}. They also offer the prospect to co-culture vascular and stromal elements and investigate
90 heterotypic interactions¹³. This is a crucial prerequisite for our model, since environment-mediated
91 drug resistance has been shown to be a major contributor to MRD¹⁴.

92 3D cell culture technologies can be classified as scaffold-free or scaffold-based. Scaffold-free
93 systems include multi-cellular aggregates formed using the hanging-drop method^{15, 16}, suspension
94 plates^{17, 18}, silicone micro-moulds¹⁹ (which can prevent cell adhesion), or spinner flasks²⁰. However,
95 the formation of cell aggregates with a large number of cells (>500 µm) requires prolonged
96 incubation over several days. Additionally, 3D microtumours fabricated by these methods often
97 exhibit significant variation in size, limiting their application in the screening of therapeutics.

98 Scaffold-based systems employ biocompatible materials, such as hydrogels, as structural
99 supports for cell culture^{8, 13}. Cells proliferate in the scaffolds and establish cell-cell and cell-ECM
100 interactions, displaying natural 3D structures instead of flattening out as they do in 2D culture²¹.
101 Despite all these advantages, the application of 3D cell culture models to drug screening has been
102 constrained by long fabrication times, poor repeatability and low productivity⁸.

103 Microfluidics is a promising tool for dealing with various unmet needs in 3D cell culture. Based
104 on the immiscibility of aqueous and oil phases, discrete aqueous droplets of uniform size and
105 composition can be generated by microfluidics, in which cells can be encapsulated in a highly
106 reproducible and high-throughput manner for subsequent 3D culture. For example, microfluidics has
107 been adopted to create organoids or tumour spheroids for predicting drug responses²², investigating
108 tumour vascularization²³, and for studying hair follicle regeneration with stem cell patterning²⁴. In the

109 present work, a microfluidics platform was established and optimised to fabricate scaffold-based 3D
110 microtumours, with readily customisable size, morphology and hydrogel choice. 3D microtumours
111 of various size were produced by this approach, and key characteristics, such as cell viability and
112 hypoxic core formation, were determined. First-line therapeutics screening was performed on
113 the 3D microtumours to demonstrate their utility in pharmacology. Finally, 3D microtumours were
114 successfully used as a drug screening platform for ovarian cancer MRD. The structures showed the
115 same molecular signatures observed in clinical MRD and led not only to the identification of a very
116 promising therapeutic agent but also to significant insight into resistance mechanisms.

117

118 Results

119 Microfluidic platform generates 3D microtumours of tailorable size, cell content, and shape

120 The 3D microtumours, tumour cells encapsulated in biocompatible hydrogels, were fabricated
121 by using a surfactant-free, droplet-based microfluidic platform (Figure 1A). Specifically, ovarian
122 cancer cells OVCAR-5/RFP were mixed with Matrigel to form the bioink ($\sim 3.5 \times 10^7$ cells mL $^{-1}$). The
123 bioink and tetradecane oil were loaded into two separate syringes and pumped into a 3-channel
124 polydimethylsiloxane (PDMS) microfluidic chip (Figure S1A), in which the two immiscible liquids met
125 and produced 3D microtumours separated by oil. The microfluidic fabrication was performed at 8°C
126 to prevent the Matrigel gelation or viscosity change. At least one hundred 3D microtumours were
127 produced within 3 minutes and temporarily stored in a polytetrafluoroethylene (PTFE) exit tube
128 (inner diameter = 900 µm) (Figure S1B) connected to the microfluidic chip. The exit tube was then
129 incubated at 37°C for 2 h to complete gelation of the Matrigel. The temperature and time required
130 for gelation varies with the hydrogel, which included collagen, agarose and silk fibroin (Table S1,
131 Figure S1C, see Methods for more details). In addition to OVCAR-5/RFP, we have also successfully
132 fabricated 3D microtumours with other tumour cell lines (OVCAR5, OVCAR8, Kuramochi, MDA-MB-
133 231, HeLa) and similar constructs from normal tissue cell lines (fibroblasts, adipocytes, embryonic

134 kidney cells) (Table S2). Cells proliferated within the 3D microtumours, which increased their density
135 by D2 (Figure 1A). Long term culture of 3D microtumours for up to 9 weeks has been achieved and
136 no major morphological changes have been observed (Figure S1D).

137 To examine if the microfluidic fabrication process had caused damage to the cells, viability
138 assays were performed at three stages of microfluidic fabrication: 2D cells harvested from culture
139 flasks, cell-hydrogel bioink, and 3D microtumours after microfluidic fabrication. Cell viabilities of >90%
140 were achieved with no significant differences observed among all the three stages, proving that the
141 microfluidic fabrication does not harm the cells. High cell viability was maintained with a variety of
142 cells (Figure 1B) and different hydrogels (Figure 1C, Table S3).

143 The microfluidic platform offers flexibility in adjusting the size, cell content and shape of 3D
144 microtumours, which is hard to achieve with other fabrication methods. By simply using PTFE exit
145 tubes with different inner diameter, 3D microtumours of different sizes (small, medium, and large)
146 can be prepared. Cell contents were managed by adjusting the ratio of different cell types during
147 bioink preparation. Three types of microtumours were fabricated: 1) OVCAR-5/RFP tumour cells
148 only; 2) 50: 50 mixture of OVCAR-5/RFP tumour cells and 3T3 fibroblast cells (co-culture); and 3)
149 3T3 fibroblast cells only. For each, the sizes of >60 microtumours were determined on the day of
150 fabrication. A histogram showed a narrow size distribution of 3D microtumours from the same batch
151 with 2-6% deviation (Figure 1D, Table S4). The narrow size distribution is essential for reliable and
152 reproducible drug screening experiments, since the cell population within each microtumour
153 depends on its size. Furthermore, different 3D microtumour shapes (sphere, ellipsoid, and rod,
154 Figure S1E) were created by varying the flowrate ratio of bioink and oil.

155

156 **3D microtumours recapitulate key physiological features of tumours**

157 Certain physical and biochemical characteristics of tumour cells are particularly difficult to
158 recreate *in vitro*, which leads to the use of sub-optimal models for drug screening and eventually

159 disappointing results from clinical trials⁶. Among these critical, and hard to model, features of
160 tumours we find low oxygen tension, or hypoxia, and cytoskeleton organisation.

161 Hypoxia contributes to reshaping of the tumour microenvironment and the development of
162 immunosuppression and chemoresistance²⁵, however, 2D monolayer cells lack the gradients of
163 oxygen required to produce hypoxia. Hypoxic cores are commonly observed in tumours with
164 diameters larger than 400-500 μm due to the deficient oxygen and nutrient levels towards the
165 centres of tumours^{26, 27}. Nevertheless, the initial size of microtumours prepared by prevailing
166 methods usually falls within the range of 100-300 μm ^{20, 28}. With the microfluidic platform developed
167 in this work, 3D microtumours with larger initial sizes can conveniently be produced. Significantly,
168 hypoxic cores were observed in large 3D microtumours (size = 825 μm) just 1 day after fabrication
169 (Figure 2A), while they were absent in small and medium size microtumours (size = 274 and 424
170 μm), which is consistent with the published literature^{26, 27}. We also confirmed the expression of key
171 hypoxia genes through immunofluorescence (Figure 2B, C) in older microtumours: at day 10 after
172 fabrication, the hypoxic core had expanded, with expression of P4HA1, VEGFA and NDRG1
173 observed very strongly in the middle of the structure and, more faintly, in some cells closer to the
174 edges. 3D spheroids prepared with other methods, such as the forced aggregation method, took
175 11-21 days to grow to a comparable size ($>800 \mu\text{m}$) and generate hypoxic cores^{27, 29}. Therefore,
176 hypoxic characteristics can be recapitulated in one-tenth of the time with the microfluidic platform.

177 Another key feature of tumour cells is their cytoskeleton organisation, which plays a crucial role
178 in cell motility, and therefore, in invasion and metastasis. More specifically, actin filaments can act
179 at different levels, from providing a connection with the ECM, to being mechanosensors and
180 signalling scaffolds³⁰, all of which are altered in cancer.

181 Several studies have reported that the actin patterns and dynamics observed in living tumours
182 are not recreated in 2D cultures or most 3D systems either³¹, especially when it comes to stress-
183 fibre structures³². To investigate whether our microtumours could recapitulate the same actin
184 distribution observed in ovarian cancer clinical samples, we used phalloidin staining on OVCAR5
185 cells grown in 2D cultures, OVCAR5 3D microtumours and High Grade Serous Ovarian Cancer

186 (HGSOC) pre-chemotherapy biopsies (Figure 2D). While the 2D cells are characterised by many
187 thin filopodia, a rich network of thick stress fibre-like actin bundles is present in both 3D microtumours
188 and HGSOC samples (which were also stained for E-cadherin to rule out any stromal contamination,
189 Figure S2).

190 To complement these imaging experiments with a full transcriptomics analysis, we conducted
191 RNA-Seq on both 2D cultures and 3D microtumours produced from three ovarian cancer cell lines
192 (OVCAR5, OVCAR8, OVCAR-5/RFP). Regardless of the cell line used, the microtumours
193 overexpressed genes that fall into several biological processes related to hypoxia (such as a 16-
194 fold enrichment for the positive regulation of VEGF production) and cell motility (Figure 3A). We then
195 analysed the expression of a nine-gene ovarian cancer-specific hypoxic signature³³ across all our
196 samples: for OVCAR5 and OVCAR-5/RFP almost all genes were consistently upregulated in the
197 microtumours (Figure 3B, C), while for OVCAR8 the upregulation was restricted to VEGF and
198 NDRG1 (Figure S3A, B).

199 On the other hand, 2D cultures were enriched for cell cycle related genes (Figure 3D, E, F),
200 consistent with the faster cell division warranted by the continuous supply of nutrients and oxygen
201 in monolayer systems.

202 As a whole these results demonstrate that our 3D microtumour system recapitulates key
203 physiological features of tumours that profoundly influence response to therapeutics, and therefore
204 should be a suitable model for drug screening.

205

206 **Responses of 3D microtumours to chemotherapy agents**

207 3D microtumours (dimension around 900 µm) composed of ovarian cancer cells were treated
208 with the first-line chemotherapeutics carboplatin and paclitaxel. Freshly prepared 3D microtumours
209 (and 2D cells as for comparison) were distributed into 96-well plates and cultured for 2 days, and
210 then exposed to serial dilutions of carboplatin or paclitaxel for 4 days (Figure S4). Cell viabilities

211 were measured at the end of the treatments and normalized to the corresponding control groups
212 treated with DMSO.

213 3D microtumours showed higher resistance compared to 2D cells for both anticancer drugs
214 (Figure 4A, B). The ovarian cancer 3D microtumours exhibited IC₅₀ values of 100 ± 12.3 µM
215 (carboplatin) and 5.3 ± 2.0 nM (paclitaxel), which were greater than 60 ± 6.1 µM (carboplatin) and
216 2.7 ± 0.9 nM (paclitaxel) for 2D cells (Figure 4C, D, Table S5).

217 In the clinic, carboplatin and paclitaxel are administered intravenously every three weeks for 8
218 cycles. Dosage of carboplatin is calculated to deliver an AUC (area under curve) of 5 (mg mL⁻¹)·min.
219 This would give a theoretical maximum plasma concentration (C_{max}) of 280 µM in a typical patient
220 (calculations in Table S6), although the true C_{max} is around 115 µM³⁴. *In vivo*, around 50% reduction
221 in the CA125 biomarker is observed with each neoadjuvant chemotherapy cycle³⁵. This response
222 aligns to the IC₅₀ for carboplatin in 3D microtumours but, by contrast, 2D monolayers are around
223 twice as sensitive. With this said, recapitulating pharmacokinetics is difficult; the *in vitro* carboplatin
224 dose to deliver the same AUC as *in vivo* would be just 6.5 µM. Moreover, *in vivo* the longevity of
225 plasma paclitaxel concentration above 50 nM is what is typically associated with clinical efficacy –
226 10-fold higher levels than observed *in vitro*³⁶.

227 Stromal cells, such as fibroblasts, are crucial components in the ovarian cancer
228 microenvironment and can regulate tumour progression³⁷. Therefore, we incorporated fibroblasts in
229 the ovarian cancer 3D microtumours (co-culture) to provide a more physiological relevant
230 microenvironment. When treated with paclitaxel, a 11-fold higher IC₅₀ value was found in co-culture
231 than in OVCAR-5/RFP tumour cells only 3D microtumours. While for 2D cultures, the IC₅₀ was only
232 2.3-fold higher in co-culture than in tumour cells only (Table S7). These IC₅₀ values indicate that
233 crosstalk between fibroblasts and tumour cells was different in 3D and 2D cultures, which may
234 contribute to therapeutic failure. Interestingly, we found more cells survived the paclitaxel treatment
235 in co-culture than in tumour cells only. To further investigate the responses to paclitaxel in co-culture,
236 a third collection of 3D microtumours that contained 3T3 fibroblasts only were fabricated. Despite
237 high concentration of up to 1000 nM was used, 47% cells in 3D microtumour and 36% cells in 2D

238 cultures survived the paclitaxel treatment. The result that 3T3 cells were not completely eliminated
239 can be attributed to the differential cytotoxicity of paclitaxel towards tumour cells over normal cells³⁸.

240 Intriguingly, distinct migration patterns were observed for co-culture 3D microtumours. OVCAR-
241 5/RFP tumour cells and 3T3 fibroblast cells were well-mixed upon fabrication and both cell types
242 were homogeneously dispersed throughout the 3D microtumour on D0. The 3T3 fibroblasts started
243 to migrate towards the periphery on D2 and clearly accumulated at the edge of the structure by D4.
244 Conversely, OVCAR-5/RFP tumour cells remained evenly distributed within the 3D microtumour
245 from D0 to D4 (Figure 4E, F, G). This observed core-shell structure may also contribute to the
246 increased IC₅₀ values for co-culture 3D microtumours than those composed of tumour cells only.

247

248 **3D microtumours as a superior model of ovarian cancer MRD**

249 After establishing that our 3D microtumour system is physiologically accurate and technically
250 sound, we sought to test whether it could be used to model a specific cancer in a practical application.

251 One of the biggest challenges in cancer research is finding new therapeutics that can eradicate
252 chemotherapy-resistant cells. This problem is especially relevant in ovarian cancer, which exhibits
253 a high recurrence rate of >80% within 18 months³⁹ due to MRD, drug resistant cells that survive first
254 line treatment and initiate relapse (Figure 5A).

255 In a previous work we described how MRD cells show distinctive features such as the
256 upregulation of cancer stem cell markers and genes involved in lipid metabolism, and a more
257 pronounced mesenchymal profile⁴. We also developed an MRD 2D *in vitro* model where treatment-
258 naïve cancer cells were exposed to carboplatin concentrations to achieve >90% cell killing; the
259 surviving cells recapitulated some of the features of MRD (such as upregulation of lipid metabolism),
260 but lacked the complexity of multicellularity and three dimensionality. Therefore, we decided to make
261 microtumours from chemotherapy-resistant cells and test their suitability as a model for
262 recapitulating MRD biology.

263 Firstly, we compared the RNA-Seq data obtained from 2D cultures and 3D microtumours to the
264 previously published libraries obtained from patients with MRD. As shown by Principal Component
265 Analysis (Figure 5B), naïve 2D cells differ most from clinical samples; MRD 2D cells and naïve 3D
266 microtumours represent an intermediate state, while MRD 3D microtumours are the most similar to
267 clinical samples, regardless of the cell line used.

268 This was confirmed by differential expression analysis, which identified fewer differentially
269 expressed genes (DEGs) between MRD 3D microtumours and clinical samples than between MRD
270 2D and clinical samples (Figure 5C). The majority of these DEGs are shared between the two
271 comparisons (Figure 5D, E). If we focus only on the genes uniquely upregulated in MRD 2D, we can
272 appreciate a significant enrichment in pathways related to cell cycle and division (Figure 5F), similar
273 to what we observed when we compared the transcriptomes of naïve 2D cultures and naïve
274 microtumours (Figure 3D).

275 Other genes exclusively enriched in MRD 2D seem to suggest a different metabolic strategy
276 between these cells and the MRD from clinical samples, with the former based on carbohydrates
277 and amino acids (Figure 5G). This was confirmed by the finding that, when we directly compared
278 the transcriptomes of MRD 2D and MRD 3D microtumours, the latter showed significant
279 upregulation of genes involved in lipid transport and metabolism (Figure 6A), similarly to what we
280 originally found in patients with MRD. Moreover, the expression of genes belonging to the original
281 MRD signature correlated significantly with the expression levels observed in the MRD 3D
282 microtumours (Pearson's correlation coefficient of 0.99, p value <0.05) (Figure S5A, B).

283 Another MRD characteristic which is better recapitulated in 3D microtumours is the increased
284 expression of ABC (ATP-binding cassette) transporters and markers for tumour initiating
285 cells/cancer stem cells (TICs/CSCs): consistent with the fact that MRD lesions survive
286 chemotherapy and are the source of ovarian cancer recurrences, we previously identified an
287 ABC/TIC/CSC gene signature which we now find overexpressed in MRD 3D microtumours
288 compared to MRD 2D (Figure 6B). Additionally, we showed that the aldehyde dehydrogenase
289 ALDH3A1, a known TIC/CSC marker which is also important for fatty acid oxidation (FAO)⁴⁰, is

290 specifically expressed in the MRD 3D microtumours but not in the naïve 3D microtumours (Figure
291 6C).

292 To further explore the nature of pathways and processes that characterise MRD cells in our
293 different models, we also conducted gene set enrichment analyses (GSEA). This identified several
294 pathways consistently downregulated in both 2D and 3D microtumours relative to clinical samples,
295 such as immunoregulatory interactions (Figure S6A, B) and genes sets associated with ECM (Figure
296 S6C, D). While the downregulation of immunoregulatory interactions is to be expected in our *in vitro*
297 models, both of which lack immune cells, it is important to note the different normalised enrichment
298 score (NES) and adjusted p values for ECM related genes in the two comparisons, pointing to a
299 much more extensive downregulation in the 2D system (Figure S6E). Moreover, the GSEA results
300 confirmed that several cell cycle and non-lipid metabolic pathways are more significantly
301 upregulated in 2D (Figure S6F).

302 Consistent with this, a recent comparison of the ovarian cancer cell line OVCAR8 in scaffolded
303 spheroids versus monolayers found that the most differentially expressed genes orchestrated
304 immune response, ECM interaction and lipid metabolism⁴¹.

305 Finally, we examined whether microtumours can recapitulate non-genetic heterogeneity, a key
306 mechanism for the evolution and survival of cancer cells. Tumour heterogeneity is both genetic and
307 non-genetic, with the latter used to describe cells of the same genetic background but with different
308 phenotypic cell states that can enable invasion, metastasis and chemotherapy resistance.

309 We previously reported that ovarian cancer non-genetic heterogeneity can be measured with
310 molecular signatures related to five different cell states (cell cycle, EMT (epithelial-mesenchymal
311 transition), KRT17, differentiated and ciliated)⁴². Deconvolution analysis of our RNA-Seq dataset
312 showed that all the five gene signatures originally identified in ovarian cancer clinical samples can
313 be found in the 3D microtumours; however, depending on the cell line, only one to three are present
314 in naïve 2D cultures and, consistent with the results we have shown so far, the most abundant is
315 related to the cell cycle state (Figure 6D). We also analysed a publicly available dataset of 37
316 additional ovarian cancer cell lines grown in 2D cultures⁴³, in all of which the cell cycle signature is

317 dominant if not exclusive (Figure S7A); hence, this is a ubiquitous drawback of monolayer cultures,
318 which all fail to recapitulate the essential features of chemoresistant cells.

319 On the other hand, 3D microtumours made from cell lines perform at least as well as organoids
320 established from clinical samples⁴⁴, where we observe the occasional sample with only the cell cycle
321 status and very low representation of the ciliated signature (Figure S7B). Furthermore, in our
322 OVCAR5 and OVCAR-5/RFP 3D microtumours, the MRD samples show a higher EMT proportion
323 than the naïve cells (Figure 6D); this is again similar to what we observed in our original
324 characterisation of MRD clinical samples⁴.

325 Taken all together, these data provide strong evidence in support of using microtumours to
326 model ovarian cancer MRD; the system successfully recapitulates most of its key features, from lipid
327 metabolism to TICs and EMT.

328

329 **Using 3D microtumours as a drug screening platform for ovarian cancer MRD**

330 3D microtumours satisfy all the technical criteria to be used as a high-throughput drug screening
331 platform and they can be considered a faithful model for ovarian cancer MRD. The next logical step
332 was to use this system to screen for compounds that can selectively target and eradicate MRD cells.

333 In our previous work we showed that not only do the MRD cells significantly upregulate their
334 lipid metabolism, but also that this is a vulnerability that can be targeted therapeutically by inhibiting
335 FAO and, in particular, by targeting the carnitine palmitoyl transferase (CPT1) that imports FA into
336 mitochondria for β-oxidation. This was achieved using our 2D model, where MRD cells treated with
337 the CPT1 inhibitors etomoxir and perhexiline underwent 20-30% more cell death than naïve cells⁴.

338 To compare the previous 2D culture data with our MRD 3D model, 3D microtumours were
339 prepared from naïve and MRD cells and treated with etomoxir and perhexiline for a period of 10
340 days (Figure S8A). By contrast with the results from 2D cultures, etomoxir failed to induce significant
341 cell death in either naïve or MRD 3D microtumours (Figure 7A), while perhexiline led to a more
342 pronounced reduction in MRD cells in 3D microtumours (Figure 7B) than in 2D cultures. Specifically,

343 in 3D microtumours, perhexiline killed MRD cells 48-82% more effectively than naïve cells,
344 depending on the cell line (Table S8).

345 This differential efficacy of FAO inhibitors in 2D cultures versus 3D microtumours could be due
346 to differences in the ability of these compounds to reach the inner cell layers of the 3D microtumours
347 or to their different selectivity (perhexiline inhibits both CPT1 and CPT2 while etomoxir only targets
348 CPT1)⁴⁵.

349 To gain more insight into this, we analysed the transcriptomes of the cells in the MRD 3D
350 microtumours that survived the treatment with the inhibitors and compared them to the
351 transcriptomes of the cells in the untreated/DMSO control MRD 3D microtumours. Differential
352 analysis showed that, regardless of the cell line, the etomoxir-resistant cells upregulated a set of
353 key genes that can increase FAO at different levels (Figure 7C, D, S8B): beside CPT1 itself, we also
354 found transcripts encoding the long-chain-fatty-acid-CoA ligase ACSL5, the very long-chain specific
355 acyl-CoA dehydrogenase ACADVL, and the pyruvate dehydrogenase kinase PDK4⁴⁶. CPT1 and
356 ACADVL upregulation in the etomoxir-resistant 3D microtumours was also confirmed at protein level
357 through immunofluorescence (Figure 7E, S9).

358 Extracting enough RNA to make libraries from the perhexiline-resistant 3D microtumours was
359 particularly challenging due to this inhibitor's strong cytotoxicity and therefore the much lower
360 number of viable cells. However, once we succeeded, the RNA-Seq analysis showed a different
361 gene signature from the etomoxir-resistant 3D microtumours, even though it was still closely linked
362 to lipid metabolism. Depending on the cell line, the cells that survived perhexiline treatment
363 upregulated at least three to five of the following genes at both the RNA and protein level: the long-
364 chain-fatty-acid-CoA ligase ACSL1, the fatty acid synthase FASN, the stearoyl-CoA desaturase
365 SCD and the aldo–keto reductases AKR1B10 and AKR1C2 (Figure 7F, G, S8C, D). While AKR1B10
366 has been shown to increase FAO in metastatic breast cancer⁴⁷, the inhibition of AKR1C1/2 can
367 sensitise platinum-resistant ovarian cancer towards carboplatin⁴⁸.

368 Overall, these data confirm once more the potential of the microtumour system, which can be
369 used not only for drug screening purposes but also to investigate resistance mechanisms. More

370 specifically, in this case, our model has enabled us to identify a very promising CPT1/2 inhibitor for
371 targeting ovarian cancer MRD as well as the key genes that we could also target simultaneously to
372 avoid the development of resistance.

373

374 **Discussion**

375 While prevention and early detection strategies are essential to improve the survival of cancer
376 patients, there is also a dire need for new therapeutics to successfully eradicate resistant cells. In
377 particular, drugs that could specifically target MRD would be extremely beneficial for women with
378 ovarian cancer, a malignancy with a ten-year survival rate of only 35%⁴⁹, much lower than the 54%
379 for all cancers combined⁵⁰.

380 In this work we describe how we have achieved the first 3D model of ovarian cancer MRD using
381 microtumours obtained by microfluidics. 3D microtumour models have gained increasing
382 significance over the past decades⁵¹. Further, the FDA Modernization Act 2.0 of December 2022
383 has eliminated the requirement for animal tests prior to clinical trials strengthening the position of
384 alternative approaches to drug evaluation⁵². This regulatory change signifies a turning away from
385 animal experiments to more effective models for drug evaluation, as over 90% of drugs reaching
386 the bedside have failed due to efficacy and safety issues^{53, 54}.

387 Here we have showed that our 3D microtumour system represents one such model which
388 satisfies all the technical and biological accuracy requirements to be successfully used in high-
389 throughput drug screening. From a technical point of view, the most important criteria are: 1) uniform
390 size; 2) uniform composition; 3) rapid fabrication; 4) ease of scalability. While uniform size and
391 composition facilitate the comparison of technical repeats, rapid fabrication reduces variations
392 arising from factors such as initial cell population differences. For example, even when cell
393 populations are nearly equalized on D0, the growth rate for each spheroid may differ, leading to
394 variability in screening results. Rapid fabrication and ease of scalability, of course, increase

395 throughput. The 3D microtumours produced by the microfluidic platform meet all the aforementioned
396 requirements, overcoming the weaknesses of conventional spheroids fabrication techniques.

397 In terms of biological accuracy, our system is able to promptly recapitulate key physiological
398 features observed *in vivo*. Firstly, 3D microtumours exhibiting hypoxia can be generated within 1
399 day of fabrication (11-21 days for other methods^{27, 29}), considerably shortening the time required for
400 high throughput assays. Secondly, the model allows an accurate representation of non-genetic
401 heterogeneity, which is now recognized to play an important role in chemotherapeutic resistance⁵⁵;
402 more specifically, our ovarian cancer 3D microtumours displayed all the molecular signatures related
403 to the five different cell states recently described as the “Oxford Classic”^{42, 56} and which is paving
404 the way to patient stratification for this malignancy.

405 Lastly, due to their ability to incorporate multiple cell types, the 3D microtumours can recreate
406 the crucial interactions between tumour cells and the microenvironment. This feature cannot be
407 recapitulated in otherwise powerful 3D cultures, like patient-derived organoids, and represents one
408 of their main disadvantages⁵⁷. As an example, we were able to use our model to co-culture ovarian
409 cancer cells and fibroblasts, and we observed the formation of a core-shell structure with fibroblasts
410 migrating and accumulating at the periphery, while the cancer cells did not exhibit a preferred
411 location, a phenomenon that can be attributed to the natural difference in migration ability of the cell
412 types⁵⁸. Ovarian cancer spheroids are known to increase density by reprogramming shell cells to
413 myofibroblasts⁵⁹. This is a form of EMT, and contributes to drug resistance. Our data indicate that
414 the recruitment of local fibroblasts may be an alternative strategy. Moreover, by incorporating
415 different combinations of additional cell species and adjusting their ratios, more complex interactions
416 can be explored with potential therapeutic value. For instance, co-cultures of patient-derived ovarian
417 cancer tumour fragments and autologous immune cells have been shown to enable personalisation
418 of immune checkpoint inhibitor therapy⁶⁰.

419 Future studies should consider adding other components of the tumour microenvironment, such
420 as adipocytes, to the 3D structure: this is because ovarian cancer is characterised by a very
421 distinctive organ tropism and very rarely spreads outside of the abdominal cavity; one of its

422 preferential metastatic sites is the omentum, where crosstalk between adipocytes and cancer cells
423 has been widely documented⁶¹. In 2D models of ovarian cancer, adipocyte co-culture confers
424 proliferative and migratory advantage, as well as resistance to cell stress⁶².

425 In their current composition, our 3D microtumours are already a superior and reliable *in vitro*
426 model for ovarian cancer MRD. Transcriptomics analysis showed that the main aspects of MRD
427 biology related to lipid metabolism and TICs are successfully recapitulated in this system, while the
428 2D model is limited by the continuous exponential growth of its entire cell population.

429 Inhibitors of FAO, such as etomoxir and perhexiline, were previously found to selectively kill
430 MRD cells in a 2D format, but to be ineffective towards naïve ovarian cancer cells⁴. When the same
431 treatment scheme was applied to 3D microtumours, surprisingly, etomoxir showed no cell killing
432 while perhexiline had a far greater cytotoxicity towards MRD cells in the 3D than the 2D format.
433 Importantly, the doses of perhexiline at which responses were observed could potentially be
434 delivered safely and locally in ovarian cancer patients using Hyperthermic Intraperitoneal
435 Chemotherapy (HIPEC). Moreover, based on our transcriptomic analysis of the very few cells
436 surviving perhexiline treatment, this population could potentially be eliminated using aldose
437 reductase inhibitors, some of which have successfully been used to reverse drug resistance in
438 prostate and colorectal cancer lines⁶³.

439

440 Conclusion

441 In this study we have developed a 3D model that faithfully recapitulates the characteristics of
442 clinical MRD and can be fabricated *in vitro* in a simple and efficient manner.

443 As a whole, our findings could lead us a step closer to personalised medicine in the treatment
444 of ovarian cancer. We can imagine a future scenario where biopsies are collected during the
445 diagnostic laparoscopy or following neoadjuvant chemotherapy and then used to create 3D
446 microtumours for the screening of different lipid metabolism inhibitors as well as resistance

447 mechanisms. Through careful regulation of microtumour size and compactness, possible in this
448 model by altering flowrate, tubing size, and cellular co-culture, drug doses could be optimised. Each
449 patient would then receive the drug cocktail that proved to be the most efficient at killing her tumour
450 cells *ex vivo*.

451 Importantly, this work also represents a crucial proof of concept for the use of 3D microtumours
452 produced by microfluidics as a drug screening platform and, given its versatility, the system could
453 potentially be applied to several different types of tumours.

454

455 Methods

456 Cell Culture

457 OVCAR5/RFP, NIH3T3/GFP, MDA-MB-231/RFP and HeLa/GFP cell lines were purchased from
458 Cell Biolabs Inc., USA. HEK293T and 3T3-L1 cell lines were purchased from ATCC. Kuramochi
459 cells were obtained from the JCRB Cell Bank. All cells except 3T3-L1 were cultured in DMEM
460 (Sigma-Aldrich, #D5796), supplemented with 10% (v/v) FBS (Sigma-Aldrich, #F7524), 2 mM
461 GlutaMAX™ Supplement (Gibco, #35050038), 0.1 mM MEM NEAA (Sigma-Aldrich, #M7145), and
462 1% (v/v) Penicillin-Streptomycin (Pen-Strep, 100 U mL⁻¹ and 100 µg mL⁻¹ respectively, Sigma-
463 Aldrich, #P4333). 3T3-L1 cells were cultured routinely in DMEM supplemented with 10% (v/v) bovine
464 calf serum (ATCC, #30-2020) and 1% (v/v) Pen-Strep. To induce differentiation of 3T3-L1 cells into
465 adipocytes, the cells were cultured in differentiation medium following an established protocol (Table
466 S9)⁶⁴.

467 Bioink Preparation

468 Matrigel® Matrix (#354234) and Collagen I (#354236) were purchased from Corning Life
469 Sciences, UK. The gels were thawed completely on ice before use. Collagen I solution (2 mg mL⁻¹)
470 was prepared by diluting Collagen I (3.78 mg mL⁻¹, 52.9 µL) with ice-cold DI-water (39.5 µL), 10X
471 DPBS (6.15 µL) and 1 N NaOH (1.2 µL). Agarose solution (2% w/v) was prepared by dissolving

472 agarose powder (Thermo Fisher, #16520050) in sterile water at 100°C, then cooled to 37°C. Silk
473 fibroin solution (50 mg mL⁻¹, Sigma-Aldrich, #5154) was thawed at 4°C and supplemented with 10
474 U mL⁻¹ horseradish peroxidase (type VI lyophilized powder, Sigma-Aldrich) and 0.4 µL mL⁻¹
475 hydrogen peroxide solution (30% w/w, Sigma Aldrich). The bioink, with cell density = 3 to 4 x 10⁷
476 cells mL⁻¹, was prepared by resuspending cell pellets in the desired pre-gel solution (Table S1).

477 **Microfluidics Platform and 3D Microtumour Fabrication**

478 The microfluidics platform was improved over work previously reported by our group⁶⁵. The
479 PDMS microfluidic chips (Figure S1A) were prepared by casting on a custom-made reverse mould,
480 which was produced by a three-dimensional printer (Solid Print3D, Formlabs) using clear resin
481 (Formlabs), and provided more choices of channel size compared to the previous method of drilling
482 holes in PDMS blocks to make the T-junction. The cell-laden bioink and the oil, tetradecane (Sigma-
483 Aldrich, #172456), were loaded into separate syringes (Figure 1), and pumped into the 3-channel
484 microfluidic chip with neMESYS syringe pumps (Cetoni, Korbussen, Germany). Droplets containing
485 cells in Matrigel, separated by the oil, were formed in a PTFE exit tube (Cole-Parmer, UK). Upon
486 complete gelation (Table S1), the 3D microtumours were ejected from the exit tube, transferred to
487 cell culture medium and maintained at 37°C, 5% CO₂. Co-culture 3D microtumours in this work
488 composed of a 50: 50 mixture of OVCAR-5/RFP tumour cells and 3T3 fibroblasts.

489 **Characterizations of 3D Microtumours**

490 **Size Distribution**

491 The 3D microtumours were imaged by using a Leica DMi8 inverted epifluorescence microscope
492 platform equipped with a Leica DFC7000 CCD camera (Leica Microsystems Ltd, UK). Images were
493 processed with Fiji ImageJ software to obtain the diameter of each 3D microtumour. For 3D
494 microtumours with the cross-section of an ellipse, the dimensions were defined as size =
495 $\sqrt{\text{Major axis} \times \text{Minor axis}}$.

496 **Cell Viability**

497 The viabilities of cells in 2D culture and bioinks were determined with a Countess™ Automated
498 Cell Counter (Invitrogen) by using 0.4% trypan blue solution (Invitrogen, #C10314).

499 The viabilities of cells in 3D microtumours were evaluated with PrestoBlue™ Cell Viability
500 Reagent (Thermo Fisher, #A13261) according to the manufacturer's instructions and fluorescence
501 intensity was measured with a microplate reader (CLARIOstar Plus, BMG LABTECH) (Table S10).

502 **Hypoxic Core Staining**

503 Image-iT™ Green Hypoxia Reagent (Thermo Fisher, #I14834) was dissolved in DMSO (Sigma-
504 Aldrich, #D8418) to prepare a 5 mM stock solution, which was added to culture medium at a final
505 concentration of 5 µM. After incubation at 37°C for 3 h, 3D microtumours were imaged with a
506 confocal laser scanning microscope (Leica TCS SP5, Leica Microsystems). A standard FITC/GFP
507 excitation/emission filter set was applied. Z-stack images were taken with an optical section
508 thickness of 10 µm. The optical z slices were projected to form 2D images using z-project in Fiji
509 ImageJ software.

510 **Anticancer Drug Responses**

511 Carboplatin powder (Cayman Chemical, #13112) was dissolved and then serially diluted with
512 sterile water to yield a range of working solutions, which were added to cell medium at a 1:20 volume
513 ratio to a maximum final concentration of 500 µM.

514 Paclitaxel powder (Invitrogen, #P3456) was dissolved and then serially diluted with DMSO to
515 yield a range of working solutions, which were added to cell medium at a 1:100 volume ratio to a
516 maximum final concentration of 1 µM.

517 For drug treatment, one microtumour or 5000 cells (2D) were seeded into each well of a 96-well
518 plate (Corning #3595). After 2 d, the medium was replaced with drug-containing medium, and the
519 treatment was continued for 4 d. PrestoBlue was used to evaluate cell viability at the end of the drug
520 treatment. For each condition, 2D cells n = 11 to 21, 3D microtumours n = 20 to 32.

521 OriginPro 2023 (OriginLab Corporation) was used to plot cell viability data and generate fitted
522 dose-response curves. The IC₅₀ values were derived from the dose-response curves at 50% cell
523 viability.

524 **Minimal Residual Disease Modelling**

525 **Preparation of MRD-like cells**

526 OVCAR5 and OVCAR8 cell lines were obtained from ATCC and cultured in RPMI 1640 (Gibco,
527 Thermo Fisher, #21875034), supplemented with 10% (v/v) FBS and 1% (v/v) Pen-Strep.

528 To prepare MRD-like cells, 2D naïve cancer cells were treated with carboplatin for 2 weeks at
529 specific optimised conditions to achieve more than 90% cell killing as previously described⁴. All the
530 cells collected on D14 were expanded for 2 to 14 days (depending on cell growth) to produce the
531 MRD cells for later use.

532 **Fatty Acid Oxidation Inhibitor Responses**

533 Etomoxir sodium salt (Stratech, #S8244-SEL) was dissolved in DMSO to prepare a 40 mM stock
534 solution, which was diluted in cell medium to a final concentration of 40 µM. Perhexiline (Cambridge
535 Bioscience, #CAY16982) was dissolved in DMSO to prepare a 4 mM perhexiline stock solution,
536 which was diluted in cell medium to a final concentration of 4 µM. DMSO was added to cell medium
537 at a 1:1000 volume ratio for the control group.

538 3D microtumours were prepared from both naïve and MRD cells. Five 3D microtumours were
539 seeded into each well of a 12-well plate on the day of fabrication and cultured with 2 mL of drug-
540 containing or DMSO-containing medium for 10 d. PrestoBlue was used to evaluate cell viability at
541 the end of the drug treatment.

542 **RNA Extraction and Library Preparation**

543 RNA was extracted with the RNAqueous-Micro Total RNA Isolation Kit (Thermo Fisher,
544 #AM1931). RNA integrity was evaluated by RIN value with the 2200 TapeStation System (Agilent
545 Technologies, Inc.) and only samples with RIN values above 7 were taken forward for library

546 preparation, which was performed using a KAPA HyperPrep Kit (Kapa Biosystems, #KR1351)
547 following the manufacturer's instructions. The libraries were evaluated by using the 2200
548 TapeStation System and then quantified with a Qubit 2.0 Fluorometer (Thermo Fisher, Invitrogen).
549 Multiplexed library pools of different samples were quantified with the KAPA Library Quantification
550 Kit (Roche) and sequenced by using 75 bp paired-end reads on the NextSeq500 platform (Illumina).

551 **Processing of RNA-Seq data**

552 Sequencing reads from FASTQ files were trimmed for adapter sequences and quality with Trim
553 Galore!, and mapped to the UCSC hg19 human genome assembly using STAR (v2.7.3a). Read
554 counts were obtained by using subread FeatureCounts (v2.0.0).

555 Differential expression analysis was carried out by using edgeR (v3.36.0). Statistical
556 overrepresentation analysis was performed with PANTHER (v17), and the threshold for significance
557 was set at FDR < 0.05.

558 Deconvolution analysis was performed as previously described⁴² in the relative mode, and thus,
559 for each tumour the scores of the 5 molecular signatures added up to 1.

560 **Study approval**

561 The HGSOC clinical samples used in this study were recruited under the Gynaecological
562 Oncology Targeted Therapy Study 01 (GO-Target-01, NHS Health Research Authority South
563 Central – Berkshire Research Ethics Committee research ethics approval 11-SC-0014) and the
564 Oxford Ovarian Cancer Predict Chemotherapy Response Trial (OXO-PCR-01, NHS Health
565 Research Authority South Central – Berkshire Research Ethics Committee research ethics approval
566 12-SC-0404). All participants involved in this study were appropriately informed and consented.

567 **Immunofluorescence staining**

568 The 3D microtumours and the clinical samples were embedded in OCT (NEG-50, Richard-Allan
569 Scientific), frozen and kept at -80°C until sectioning. 10 µm sections were taken in a CryoStar
570 cryostat microtome (Thermo Fisher) and stained for immunofluorescence imaging. The slides were

571 washed with ice-cold PBS twice to remove the OCT, fixed in 4% PFA for 10 min and permeabilized
572 with 0.1%TritonX-100 in PBS for 10 min at RT. The samples were then incubated in Blocking Buffer
573 (2% BSA + 0.1% TritonX-100 in PBS) for 1 hour followed by an overnight incubation with the diluted
574 primary antibodies (Table S11) in a humidified chamber at 4°C. The following day the slides were
575 washed in PBS and incubated with the secondary antibodies and phalloidin for 1 hour at RT. After
576 extensive washes in PBS, the slides were mounted with Vectashield + DAPI (VectorLaboratories)
577 and dried in the dark before being imaged using a confocal microscope (Zeiss900).

578

579

580

Abbreviations

2D	Two-dimensional
3D	Three-dimensional
ABC	ATP-binding cassette
ATCC	American Type Culture Collection
AUC	Area under curve
BSA	Bovine serum albumin
CPT	Carnitine palmitoyl transferase
CSCs	Cancer stem cells
DAPI	4',6-diamidino-2-phenylindole
DEGs	Differentially expressed genes
DMEM	Dulbecco's modified Eagle's medium
DMSO	Dimethyl sulfoxide
ECM	Extracellular matrix
EMT	Epithelial-mesenchymal transition
FA	Fatty acid
FAO	Fatty acid oxidation
FBS	Fetal bovine serum
FDA	Food and Drug Administration
GSEA	Gene set enrichment analyses
HGSOC	High Grade Serous Ovarian Cancer
HIPEC	Hyperthermic Intraperitoneal Chemotherapy
ID	Inner diameter
JCRB	Japanese Collection of Research Biosources
MRD	Minimal Residual Disease
NEAA	Non-Essential Amino Acids
NES	Normalised enrichment score
OCT	Optimal cutting temperature
PBS	Phosphate-buffered saline
PDMS	Polydimethylsiloxane
Pen-Strep	Penicillin-Streptomycin
PFA	Paraformaldehyde
PTFE	Polytetrafluoroethylene
RT	Room temperature
TICs	Tumour initiating cells

581

582 Acknowledgements

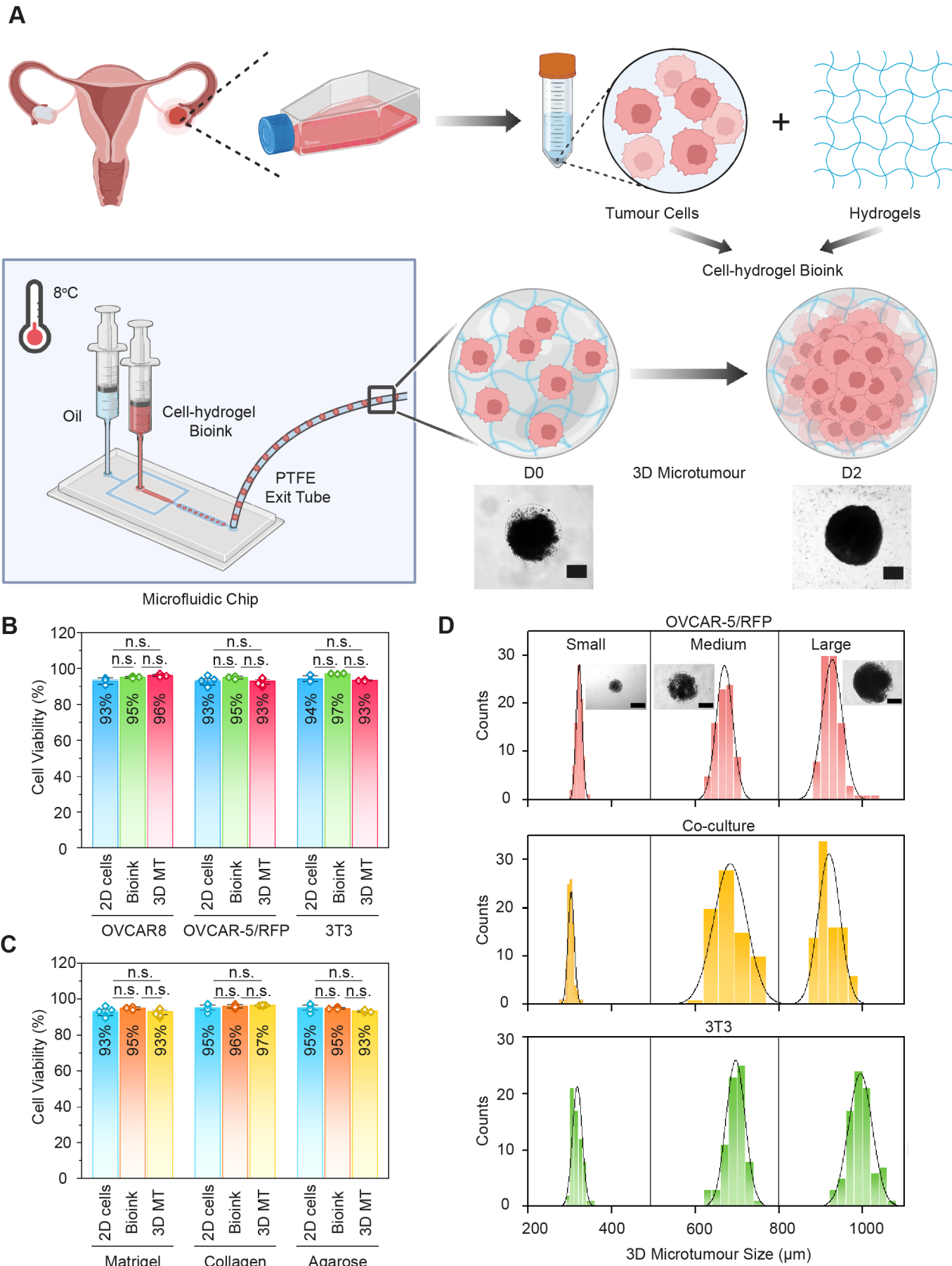
583 Work in the HB laboratory was supported by a European Research Council Advanced Grant
584 (SYNTISU) and a Proof of Concept Grant (BIOELECTRIC), and the Oxford Martin School
585 Programme on 3D Printing for Brain Repair, and a Cancer Research UK's Pioneer Award Grant
586 (CRUK). Work in the AAA laboratory was funded by Ovarian Cancer Action, the Cancer Research
587 UK Oxford Centre and the Medical and Life Sciences Translational Fund of the University of Oxford.
588 R.K.K. was funded by the Health Research Bridging Salary Scheme (0011044) at the University of
589 Oxford. The authors extend their appreciation to the Deputyship for Research & Innovation, Ministry
590 of Education in Saudi Arabia for funding this research work through the project number 852.

591

592 Author contributions

593 X.Y., M.A., H.B. and A.A.A. conceived and designed the work, which was supervised by H.B.
594 and A.A.A. X.Y. improved the microfluidic platform, and performed 3D microtumour fabrication and
595 chemotherapy assays. X.Y. and M.A. contributed to cell culture and manipulation, microscope
596 imaging, cryo-sectioning, RNA-Seq library preparation and data and image analysis. M.A.
597 performed the bioinformatics analysis and immunofluorescence. L.R. performed the deconvolution
598 analysis. Y.J. and L.Z. contributed to cryo-sectioning and cell staining. Y.Z. contributed to the
599 preparation of silk fibroin and reverse moulds of microfluidic chips. E.M. contributed to cell
600 monolayer culture. N.M. assisted with preliminary experiments on chemotherapeutic screening.
601 R.K.K., S.M., A. Aggarwal and L.Z. contributed discussions and helped with image analysis.
602 A. Albhukari contributed discussions. X.Y., M.A., A. Aggarwal, H.B. and A.A.A. wrote the manuscript.
603 H.B., A.A.A., L.Z. and M.A. acquired funding. All authors read and revised the manuscript.

604



605

606

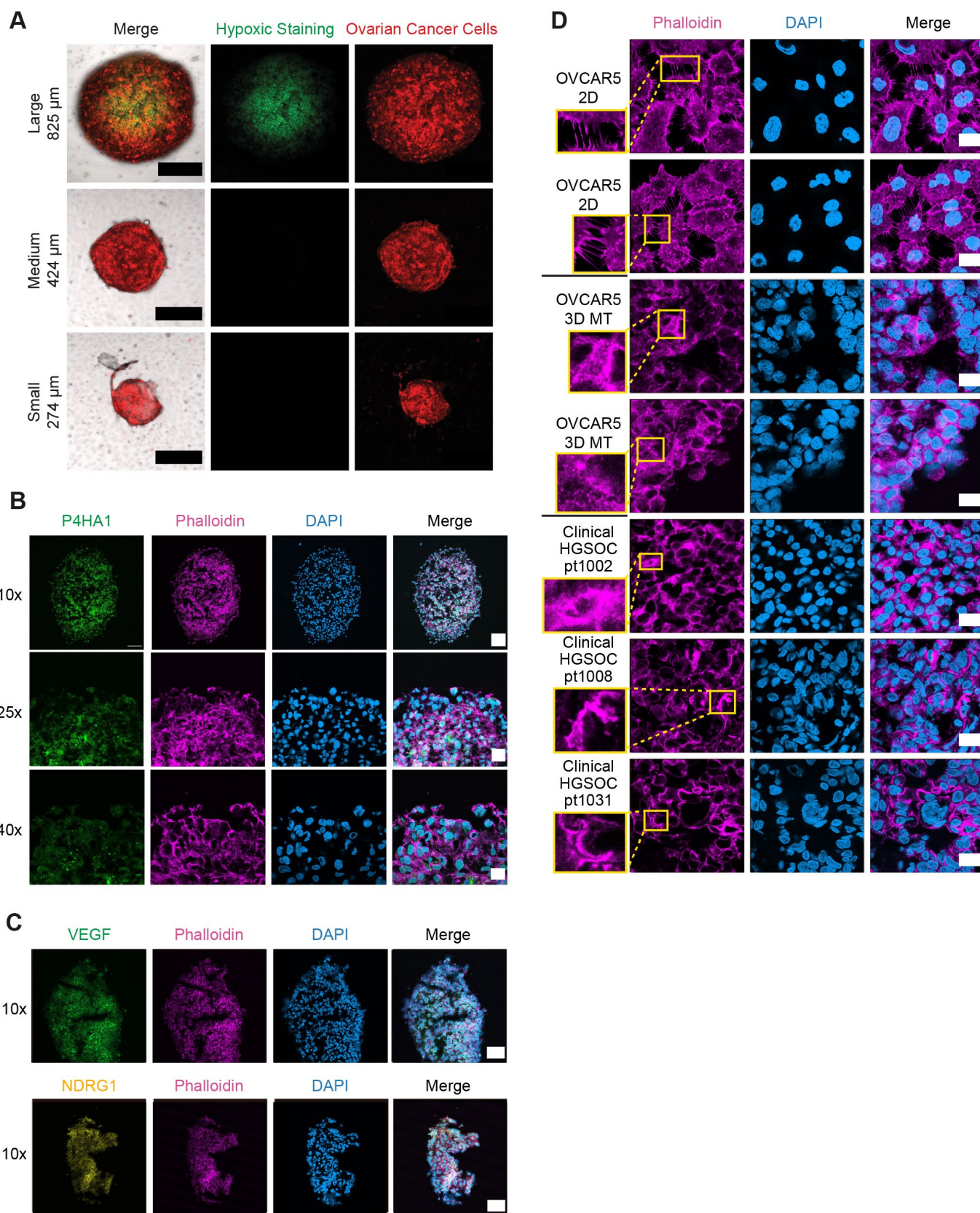
607

Figure 1. Schematic illustration and features of 3D microtumour fabrication by the microfluidic platform. A) 2D monolayer cells (ovarian cancer cells) were harvested and mixed with

608 hydrogel (Matrigel) to form a bioink. The cell-hydrogel bioink and tetradecane oil were pumped into
609 a PDMS microfluidic chip at 8°C by syringe pumps. At least one hundred 3D microtumours
610 separated by oil were generated within 3 minutes and temporarily stored in a PTFE exit tube. Upon
611 complete gelation, the 3D microtumours were transferred from the PTFE tube to a medium-
612 containing culture plate for further use. Inset: Microscope images of 3D microtumours composed of
613 OVCAR-5/RFP and Matrigel on D0 and D2 of fabrication. Scale bar = 300 µm. The diagrams were
614 created with BioRender.com. B) Cell viability at three stages of microfluidic fabrication: 2D cells
615 harvested from flasks, bioink made from cells and Matrigel, and 3D microtumours after microfluidic
616 fabrication (3D MT). Data for three cell lines are shown: OVCAR8, OVCAR-5/RFP and 3T3
617 fibroblasts (n = 3 to 6). C) Cell viability at the three stages of microfluidic fabrication for OVCAR8
618 cells with three hydrogels: Matrigel, collagen and agarose (n = 3 to 6). D) Size distributions of
619 Matrigel 3D microtumours composed of OVCAR-5/RFP tumour cells, a 50: 50 mixture of OVCAR-
620 5/RFP cells and 3T3 cells (co-culture) and 3T3 fibroblast cells (n = 62 to 90). Inset: microscope
621 images of 3D microtumours generated with PTFE exit tubes of ID = 300, 650 and 900 µm. Scale
622 bar = 300 µm.

623

624



625

626

627

628

629

Figure 2. 3D microtumours recapitulate key physiological features of cancers. A)

Epifluorescence images of hypoxia staining (green) for large, medium and small 3D microtumours

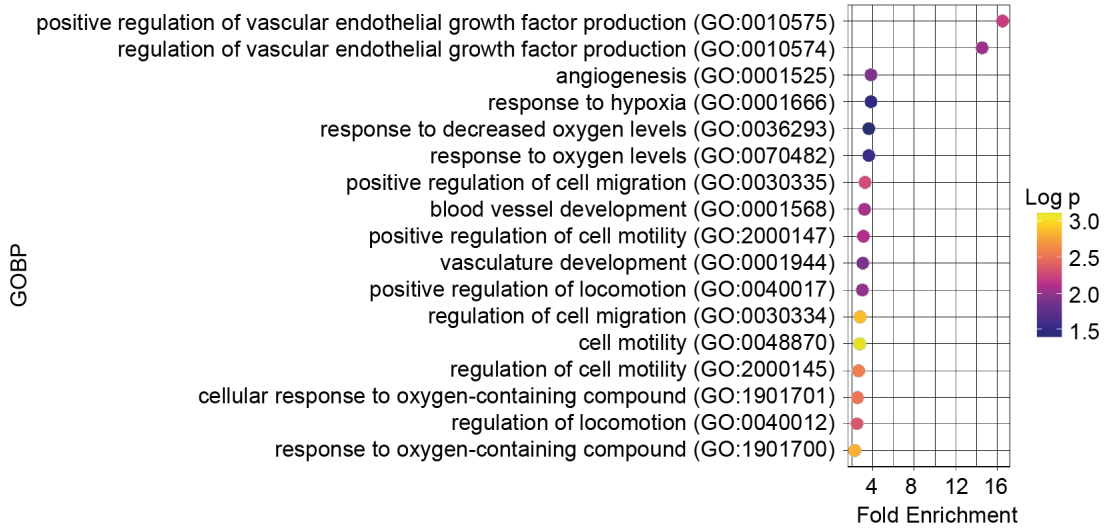
composed of OVCAR-5/RFP ovarian cancer cells (red) and Matrigel. Scale bar = 300 µm. B)

Confocal images of 3D microtumours composed of OVCAR5 ovarian cancer cells and Matrigel at

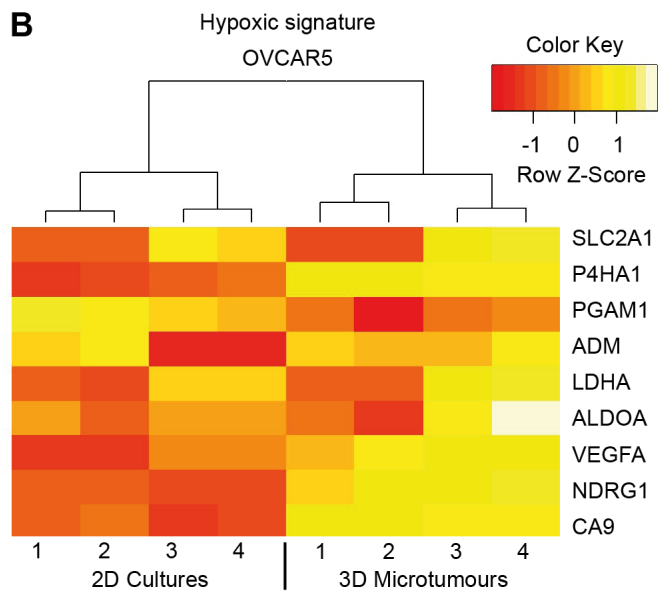
630 D10 stained with P4HA1 (green), phalloidin (pink), DAPI (blue). Scale bar = 100 µm for 10x, 30 µm
631 for 25x, and 20 µm for 40x magnification. C) Confocal images of 3D microtumours composed of
632 OVCAR5 ovarian cancer cells and Matrigel at D10 stained with VEGF (green), NDRG1 (yellow),
633 phalloidin (pink), DAPI (blue). Scale bar = 100 µm. D) Confocal images of 2D cultures (OVCAR5),
634 3D microtumours (3D MT, OVCAR5) at D10, and clinical samples stained with phalloidin (pink),
635 DAPI (blue). Scale bar = 20 µm. Inset: zoom-in images for regions of interest stained with phalloidin.

636

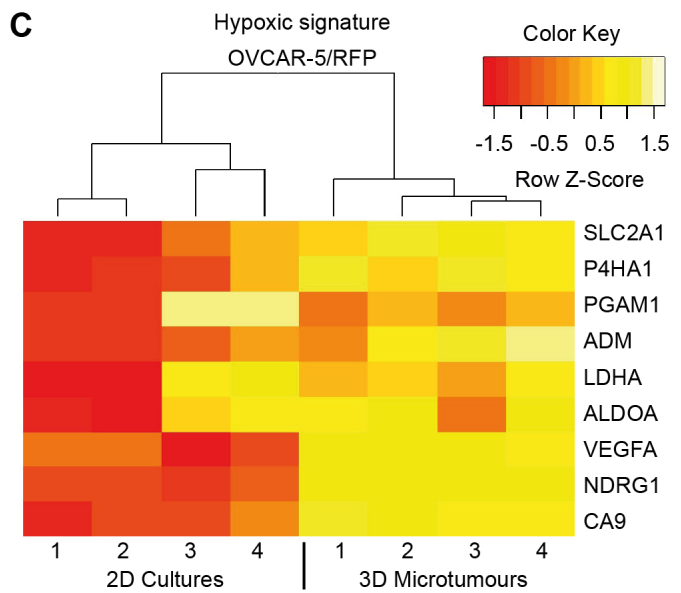
A



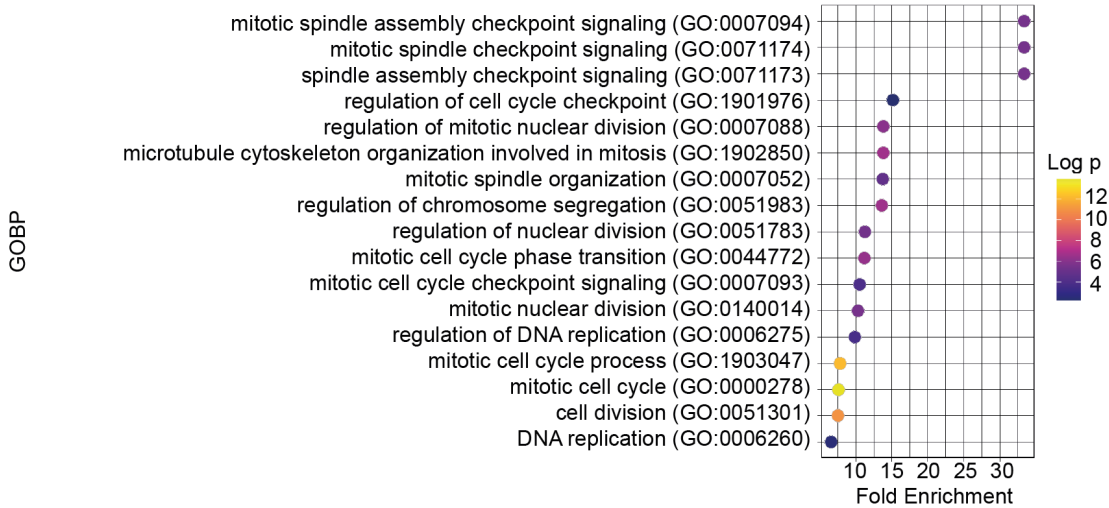
B



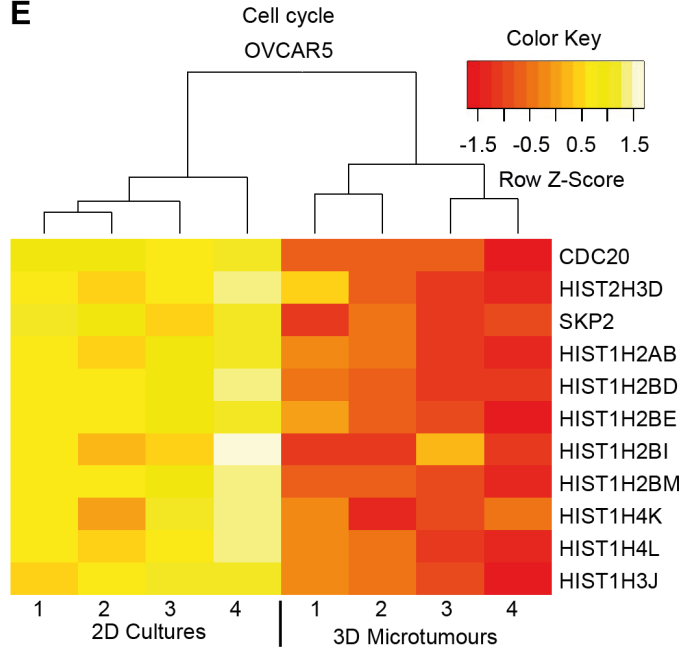
C



D

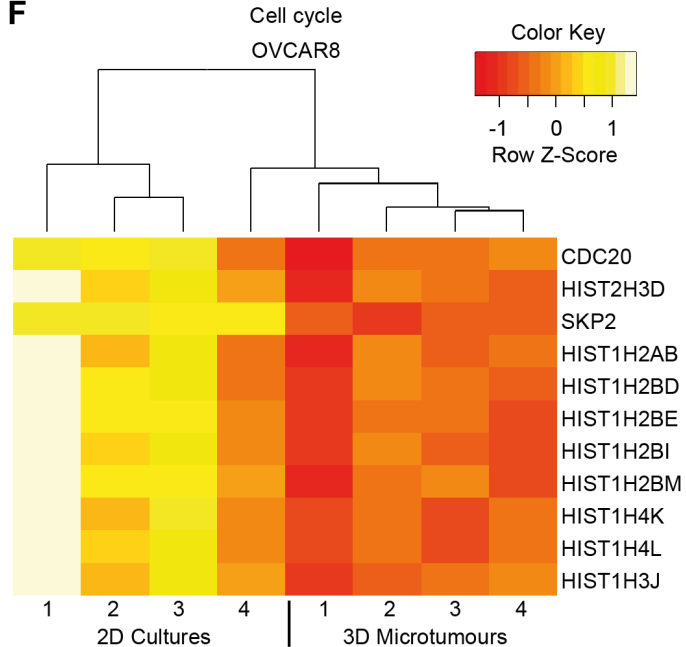


E



638

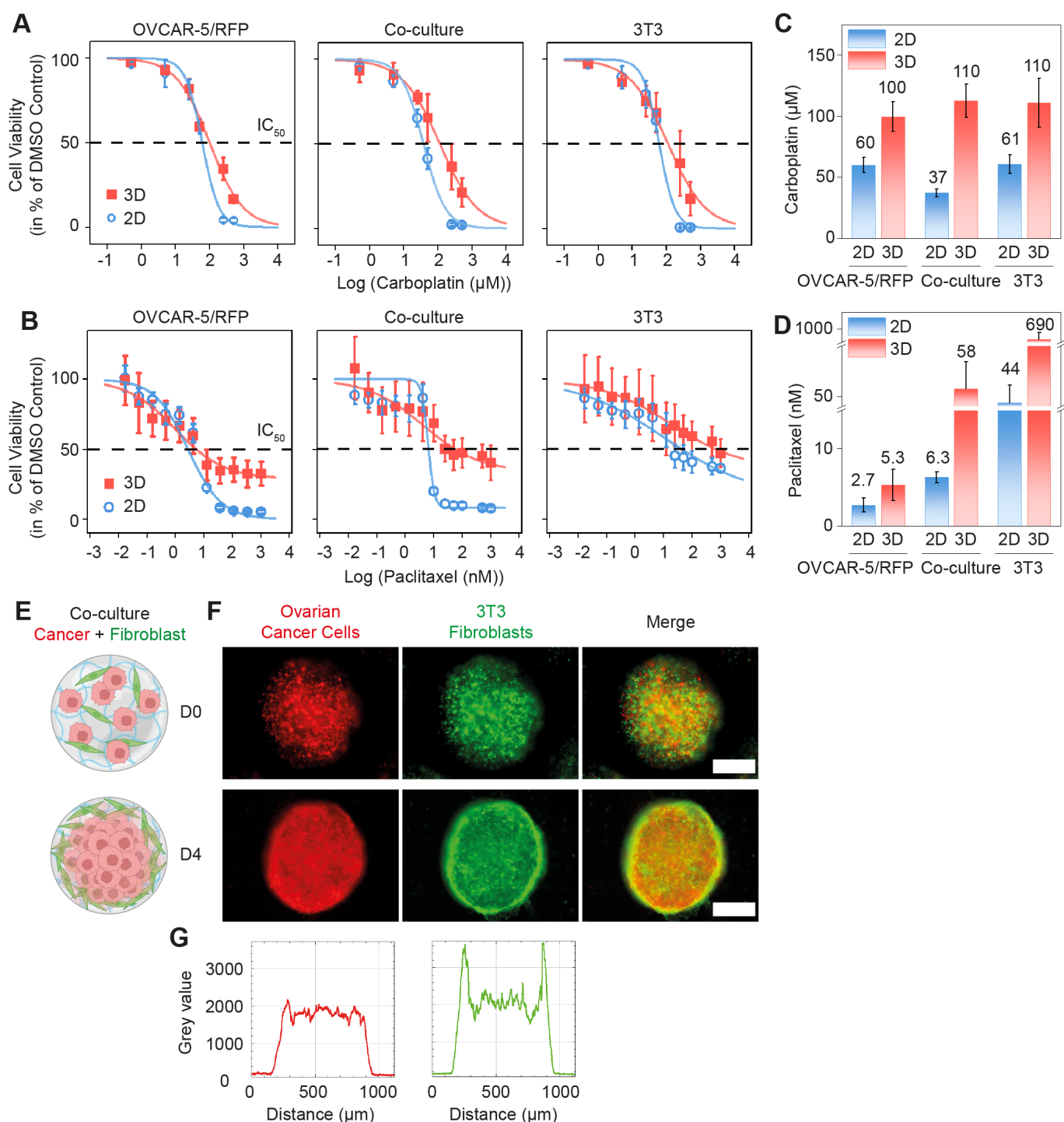
F



639

Figure 3. Transcriptomic analysis of 2D cultures and 3D microtumours. Dot plots showing the main biological processes enriched in A) 3D microtumours and D) 2D cultures produced from OVCAR5, OVCAR8 and OVCAR-5/RFP cells. Heatmaps showing the expression of an ovarian cancer specific hypoxic signature in B) OVCAR5 and C) OVCAR-5/RFP. Heatmaps showing the expression of cell cycle related genes in E) OVCAR5 and F) OVCAR8.

644



645

646 **Figure 4. Dose-response of 3D microtumours fabricated by the microfluidic platform.** Dose-
 647 response curves of 3D microtumours (pink) and 2D cells (blue) treated with serial dilutions of A)
 648 carboplatin and B) paclitaxel. Bar graphs of IC₅₀ values calculated from the dose-response curves
 649 for C) carboplatin and D) paclitaxel. E) Schematic diagram of co-culture 3D microtumours composed
 650 of tumour cells and fibroblasts at D0 and D4. The diagrams were created with BioRender.com. F)
 651 Epifluorescence images of co-culture 3D microtumours composed of OVCAR-5/RFP and 3T3
 652 fibroblasts on D0 and D4 of fabrication. Scale bar = 300 μm. G) Fluorescence intensity profile of a

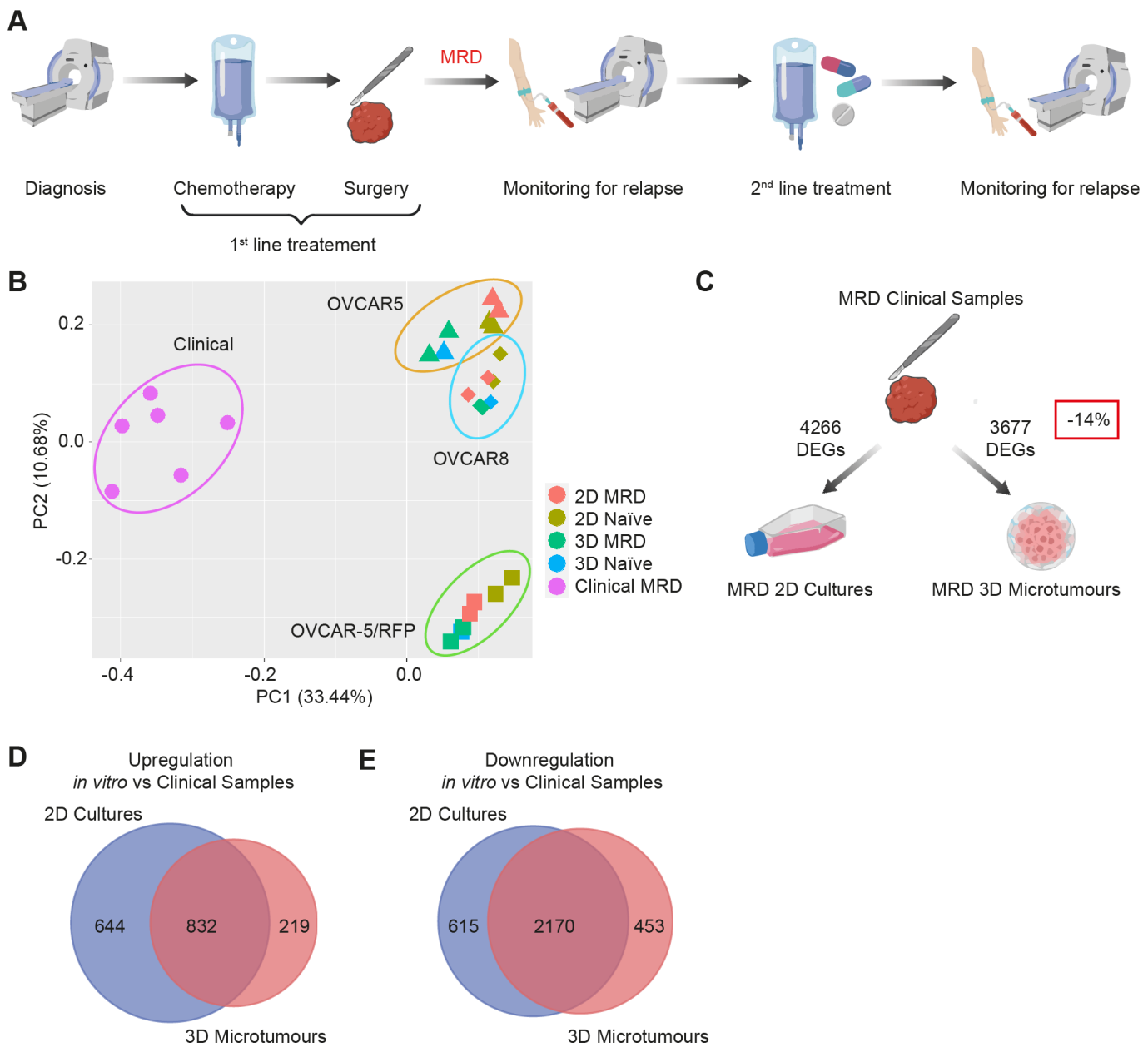
653 line across the co-culture 3D microtumour on D4. Left for OVCAR-5/RFP (red) and right for 3T3

654 fibroblasts (green).

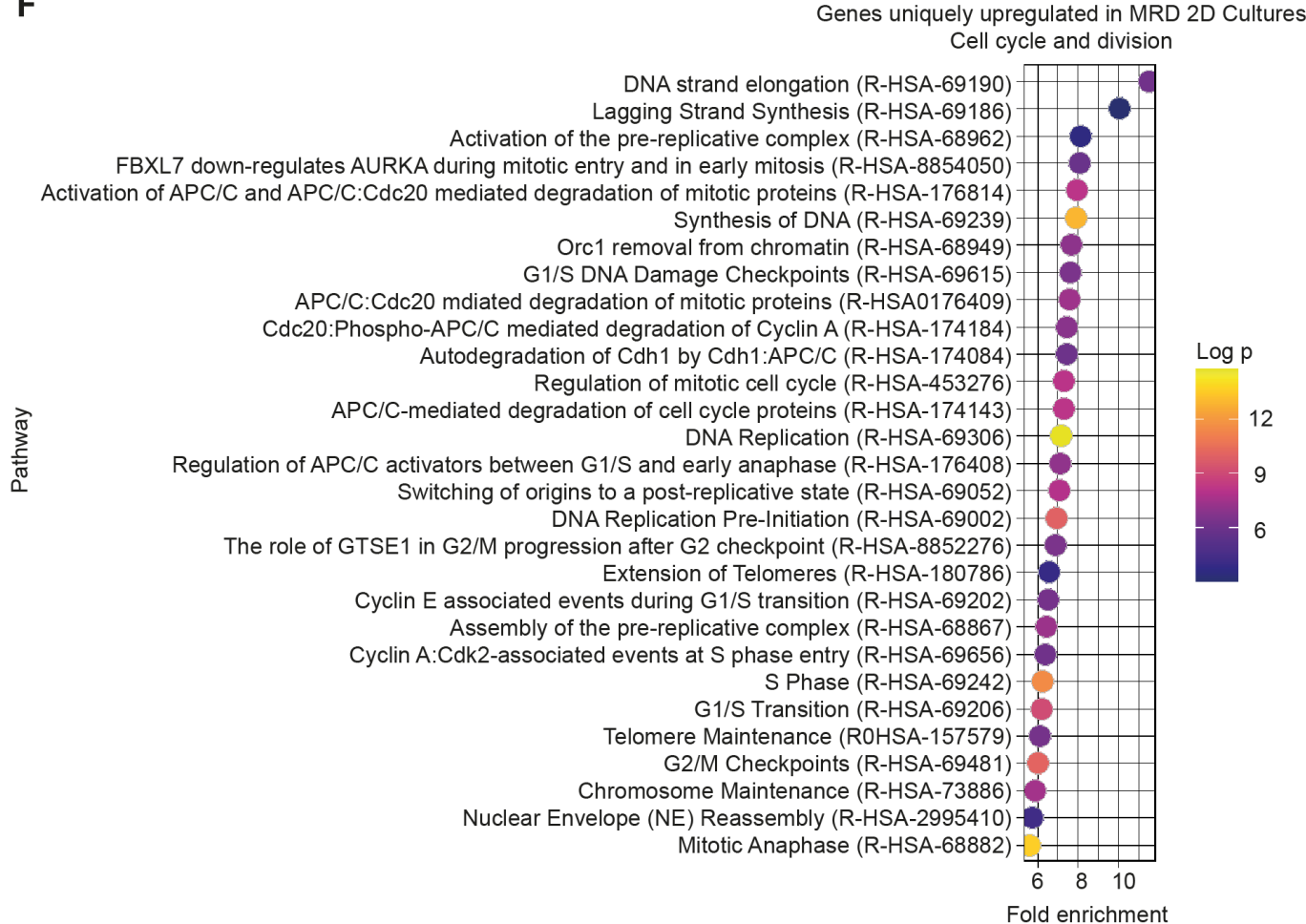
655

656

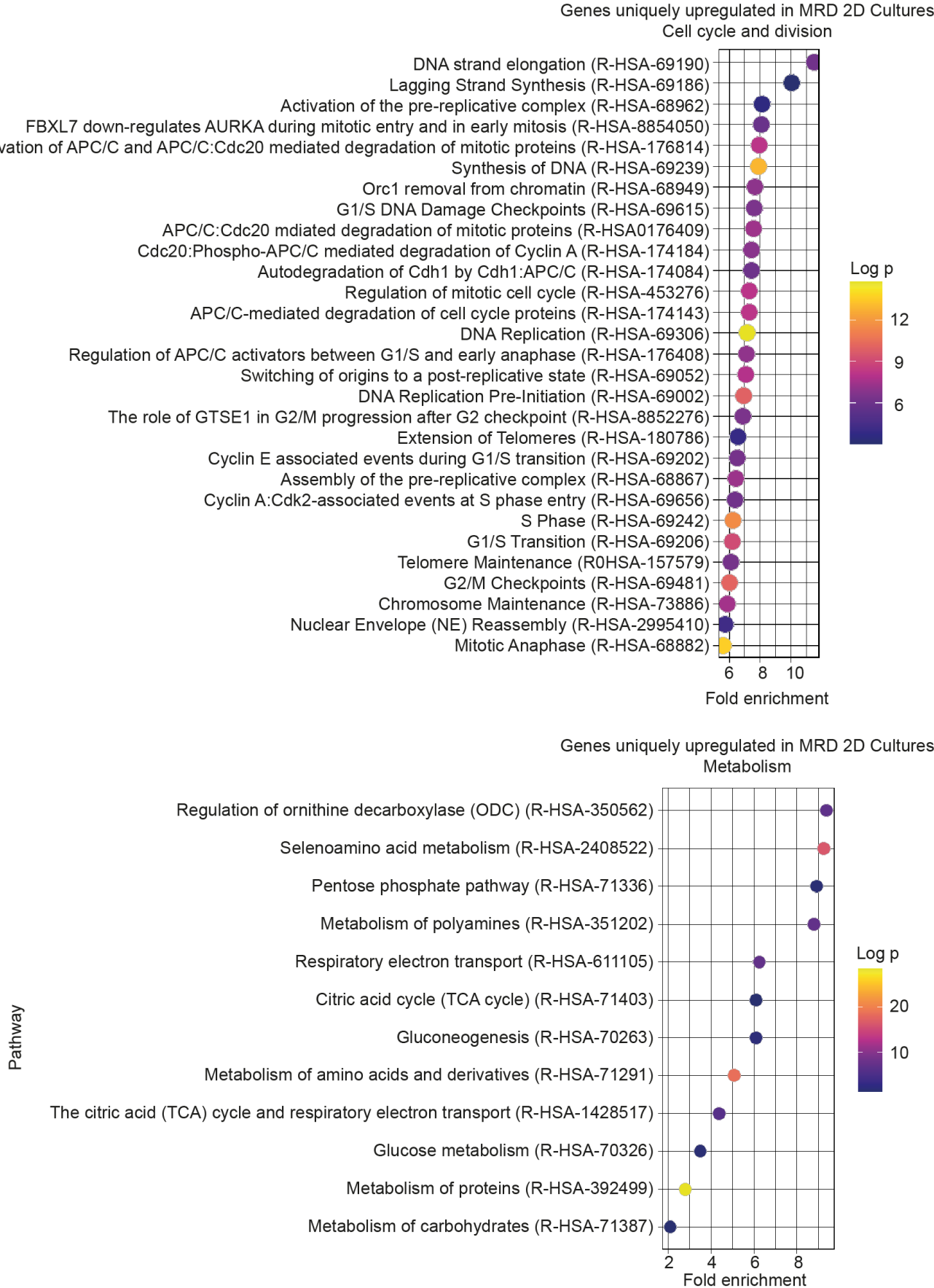
657



F



G

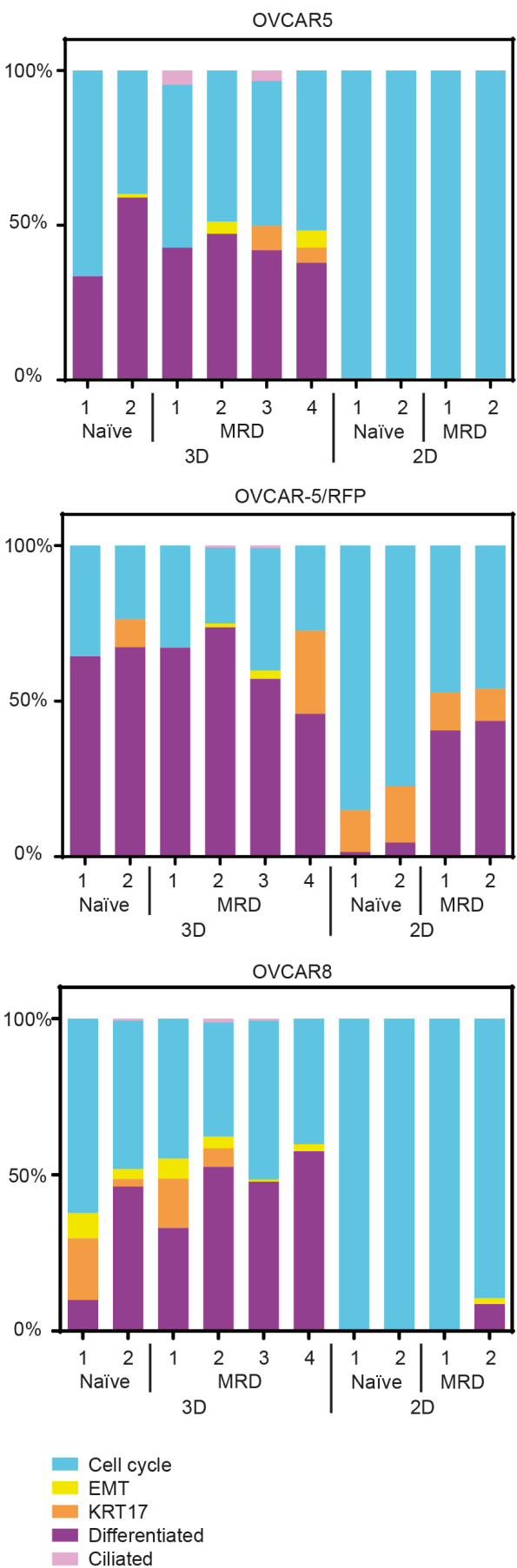
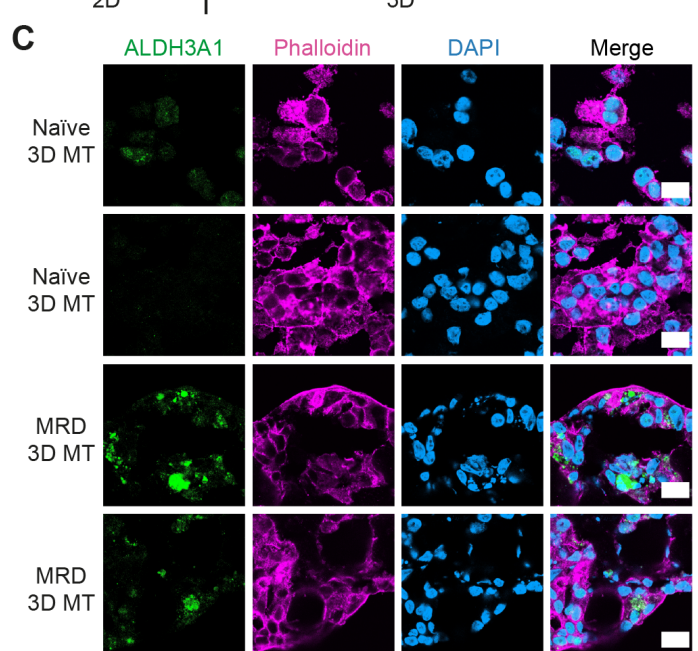
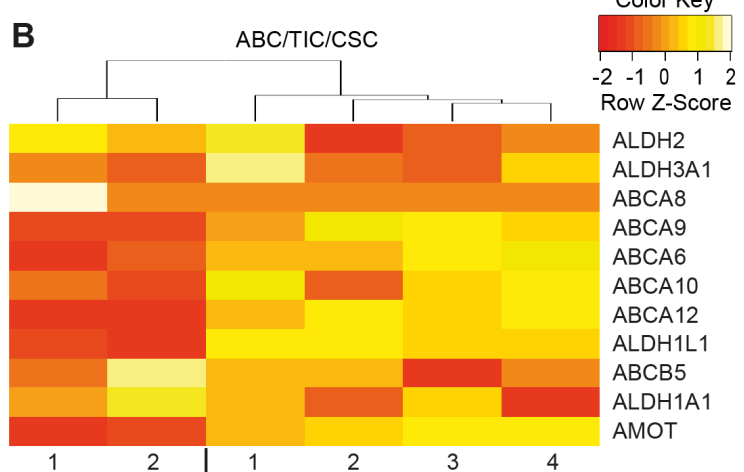
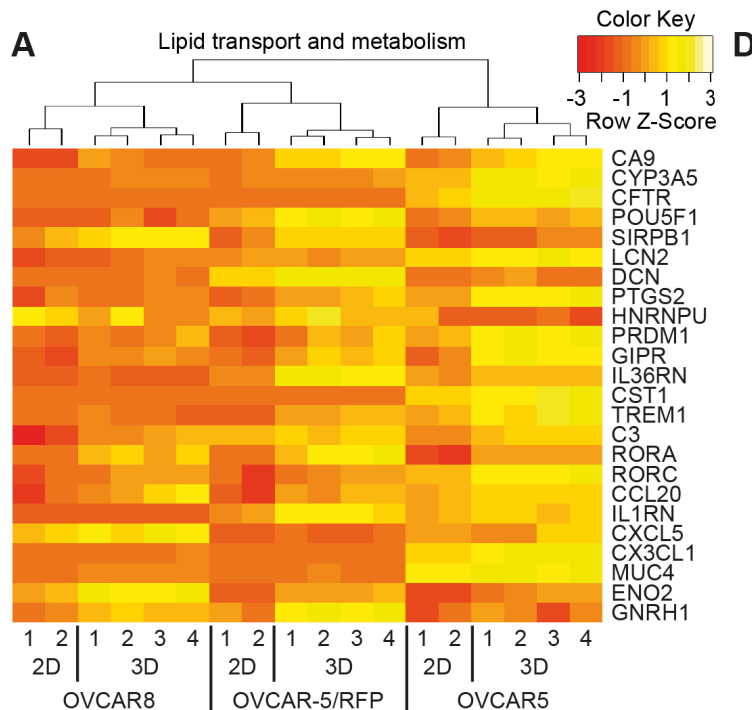


659

660 **Figure 5. 3D microtumours as a superior model of ovarian cancer MRD.** A) Schematic diagram
661 of the standard clinical management of patients with ovarian cancer. The diagrams were created

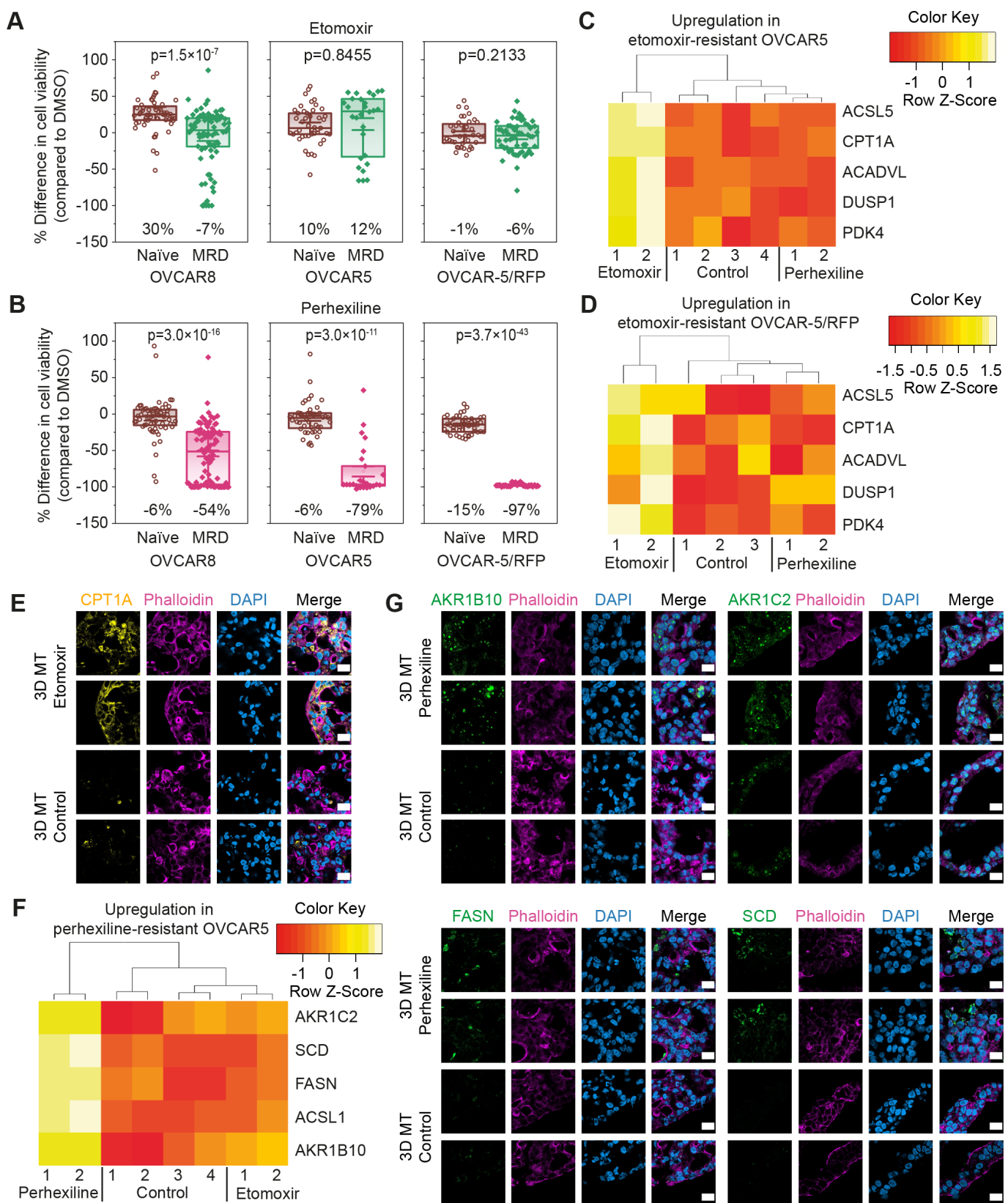
662 with BioRender.com. B) Principal component analysis plots of RNA-Seq data showing 2D cultures,
663 3D microtumours and the previously published libraries obtained from patients with MRD. C)
664 Number of differentially expressed genes (DEGs) between MRD 2D cultures or MRD 3D
665 microtumours compared to clinical samples. The diagrams were created with BioRender.com.
666 Overlap of DEGs in MRD 2D cultures or MRD 3D microtumours compared to clinical samples for
667 genes that were D) upregulated and E) downregulated *in vitro*. Dot plots showing pathways enriched
668 among genes uniquely upregulated in MRD 2D compared to clinical samples and related to F) cell
669 cycle and division, G) metabolism.

670



672 **Figure 6. Key features of ovarian cancer MRD recapitulated in 3D microtumours.** Heatmap
673 showing the expression of genes in 3D microtumours and 2D cultures A) involved in lipid transport
674 and metabolism, and B) encoding ABC transporters and markers for tumour initiating cells/cancer
675 stem cells (TICs/CSCs). C) Confocal images of 3D microtumours (3D MT) at D10 stained with the
676 TIC/CSC marker: ALDH3A1 (green), phalloidin (pink), DAPI (blue). Scale bar = 20 µm. D) Stacked
677 bar plots visualizing the deconvolution result of 3D microtumours and 2D cultures produced from
678 OVCAR5, OVCAR-5/RFP and OVCAR8. The y axis represents the percentage of each cell state in
679 a given sample. Colours of the bars denote the 5 cell states as shown in the legend.

680



681

682

683

684

685

Figure 7. 3D microtumours as a drug screening platform for ovarian cancer MRD. Cell viability changes of naïve and MRD 3D microtumours compared to a DMSO control after a 10 d treatment with A) 40 μ M etomoxir; B) 4 μ M perhexiline ($n = 25$ to 93). Heatmaps of differentially expressed genes (DEGs) upregulated in etomoxir-resistant MRD 3D microtumours composed of C) OVCAR5

686 and D) OVCAR-5/RFP. E) Confocal images of 3D microtumours (3D MT) at D10 stained with the
687 FAO marker CPT1A (yellow), phalloidin (pink), DAPI (blue). Scale bar = 20 µm. F) Heatmap of DEGs
688 upregulated in perhexiline-resistant MRD 3D microtumours composed of OVCAR5. G) Confocal
689 images showing the DEGs upregulated in perhexiline-resistant MRD 3D microtumours composed
690 of OVCAR5 at day 10: AKR1B10 (green, top left panel), AKR1C2 (green, top right panel), FASN
691 (green, bottom left panel), SCD (green, bottom right panel), phalloidin (pink), DAPI (blue). Scale bar
692 = 20 µm.

693
694

695 References

- 696 1. Ramos, A.; Sadeghi, S.; Tabatabaeian, H., Battling Chemoresistance in Cancer: Root Causes and Strategies
697 to Uproot Them. *International Journal of Molecular Sciences* **2021**, 22 (17), 9451.
- 698 2. Luskin, M. R.; Murakami, M. A.; Manalis, S. R.; Weinstock, D. M., Targeting minimal residual disease: a path
699 to cure? *Nature Reviews Cancer* **2018**, 18 (4), 255-263.
- 700 3. Bivona, T. G.; Doebele, R. C., A framework for understanding and targeting residual disease in oncogene-driven
701 solid cancers. *Nature Medicine* **2016**, 22 (5), 472-478.
- 702 4. Artibani, M.; Masuda, K.; Hu, Z.; Rauher, P. C.; Mallett, G.; Wietek, N.; Morotti, M.; Chong, K.;
703 KaramiNejadRanjbar, M.; Zois, C. E.; Dhar, S.; El-Sahhar, S.; Campo, L.; Blagden, S. P.; Damato, S.; Pathiraja, P.
704 N.; Nicum, S.; Gleeson, F.; Laios, A.; Alsaadi, A.; Santana Gonzalez, L.; Motohara, T.; Albukhari, A.; Lu, Z.; Bast,
705 R. C., Jr.; Harris, A. L.; Ejsing, C. S.; Klemm, R. W.; Yau, C.; Sauka-Spengler, T.; Ahmed, A. A., Adipocyte-like
706 signature in ovarian cancer minimal residual disease identifies metabolic vulnerabilities of tumor-initiating cells. *JCI
707 Insight* **2021**, 6 (11), e147929.
- 708 5. Johnson, P. A.; Giles, J. R., The hen as a model of ovarian cancer. *Nature Reviews Cancer* **2013**, 13 (6), 432-
709 436.
- 710 6. Asghar, W.; El Assal, R.; Shafiee, H.; Pitteri, S.; Paulmurugan, R.; Demirci, U., Engineering cancer
711 microenvironments for in vitro 3-D tumor models. *Materials Today* **2015**, 18 (10), 539-553.
- 712 7. Duval, K.; Grover, H.; Han, L.-H.; Mou, Y.; Pegoraro, A. F.; Fredberg, J.; Chen, Z., Modeling Physiological
713 Events in 2D vs. 3D Cell Culture. *Physiology* **2017**, 32 (4), 266-277.
- 714 8. Kapałczyńska, M.; Kolenda, T.; Przybyła, W.; Zajączkowska, M.; Teresiak, A.; Filas, V.; Ibbs, M.; Bliźniak,
715 R.; Łuczewski, Ł.; Lamperska, K., 2D and 3D cell cultures – a comparison of different types of cancer cell cultures.
716 *Archives of Medical Science* **2018**, 14 (4), 910-919.
- 717 9. Velletri, T.; Villa, C. E.; Cilli, D.; Barzaghi, B.; Lo Riso, P.; Lupia, M.; Luongo, R.; Lopez-Tobon, A.; De
718 Simone, M.; Bonnal, R. J. P.; Marelli, L.; Piccolo, S.; Colombo, N.; Pagani, M.; Cavallaro, U.; Minucci, S.; Testa, G.,
719 Single cell-derived spheroids capture the self-renewing subpopulations of metastatic ovarian cancer. *Cell Death &
720 Differentiation* **2022**, 29 (3), 614-626.
- 721 10. Jensen, C.; Teng, Y., Is It Time to Start Transitioning From 2D to 3D Cell Culture? *Frontiers in Molecular
722 Biosciences* **2020**, 7, 33.
- 723 11. Xu, G.; Yin, F.; Wu, H.; Hu, X.; Zheng, L.; Zhao, J., In vitro ovarian cancer model based on three-dimensional
724 agarose hydrogel. *Journal of Tissue Engineering* **2014**, 5, 2041731413520438.
- 725 12. Blanco-Fernandez, B.; Gaspar, V. M.; Engel, E.; Mano, J. F., Proteinaceous Hydrogels for Bioengineering
726 Advanced 3D Tumor Models. *Advanced Science* **2021**, 8 (4), 2003129.
- 727 13. Rojek, K. O.; Ćwiklińska, M.; Kuczak, J.; Guzowski, J., Microfluidic Formulation of Topological Hydrogels for
728 Microtissue Engineering. *Chemical Reviews* **2022**, 122 (22), 16839-16909.
- 729 14. Meads, M. B.; Gatenby, R. A.; Dalton, W. S., Environment-mediated drug resistance: a major contributor to
730 minimal residual disease. *Nature Reviews Cancer* **2009**, 9 (9), 665-674.

- 731 15. Koledova, Z., 3D Cell Culture: An Introduction. In *3D Cell Culture: Methods and Protocols*, Koledova, Z., Ed.
732 Springer New York: New York, NY, 2017; pp 1-11.
- 733 16. Badea, M. A.; Balas, M.; Dinischiotu, A., Biological properties and development of hypoxia in a breast cancer
734 3D model generated by hanging drop technique. *Cell Biochemistry and Biophysics* **2022**, *80* (1), 63-73.
- 735 17. Foglietta, F.; Canaparo, R.; Muccioli, G.; Terreno, E.; Serpe, L., Methodological aspects and pharmacological
736 applications of three-dimensional cancer cell cultures and organoids. *Life Sciences* **2020**, *254*, 117784.
- 737 18. Vinci, M.; Gowan, S.; Boxall, F.; Patterson, L.; Zimmermann, M.; Court, W.; Lomas, C.; Mendiola, M.;
738 Hardisson, D.; Eccles, S. A., Advances in establishment and analysis of three-dimensional tumor spheroid-based
739 functional assays for target validation and drug evaluation. *BMC Biology* **2012**, *10* (1), 29.
- 740 19. Zuppinger, C., 3D Cardiac Cell Culture: A Critical Review of Current Technologies and Applications. *Frontiers*
741 in *Cardiovascular Medicine* **2019**, *6*, 87.
- 742 20. Breslin, S.; O'Driscoll, L., Three-dimensional cell culture: the missing link in drug discovery. *Drug Discovery*
743 Today **2013**, *18* (5), 240-249.
- 744 21. Knight, E.; Przyborski, S., Advances in 3D cell culture technologies enabling tissue-like structures to be created
745 in vitro. *Journal of Anatomy* **2015**, *227* (6), 746-756.
- 746 22. Jiang, S.; Zhao, H.; Zhang, W.; Wang, J.; Liu, Y.; Cao, Y.; Zheng, H.; Hu, Z.; Wang, S.; Zhu, Y.; Wang,
747 W.; Cui, S.; Lobie, P. E.; Huang, L.; Ma, S., An Automated Organoid Platform with Inter-organoid Homogeneity and
748 Inter-patient Heterogeneity. *Cell Reports Medicine* **2020**, *1* (9), 100161.
- 749 23. Hu, Z.; Cao, Y.; Galan, E. A.; Hao, L.; Zhao, H.; Tang, J.; Sang, G.; Wang, H.; Xu, B.; Ma, S., Vascularized
750 Tumor Spheroid-on-a-Chip Model Verifies Synergistic Vasoprotective and Chemotherapeutic Effects. *ACS Biomaterials*
751 *Science & Engineering* **2022**, *8* (3), 1215-1225.
- 752 24. Cao, Y.; Tan, J.; Zhao, H.; Deng, T.; Hu, Y.; Zeng, J.; Li, J.; Cheng, Y.; Tang, J.; Hu, Z.; Hu, K.; Xu, B.;
753 Wang, Z.; Wu, Y.; Lobie, P. E.; Ma, S., Bead-jet printing enabled sparse mesenchymal stem cell patterning augments
754 skeletal muscle and hair follicle regeneration. *Nature Communications* **2022**, *13* (1), 7463.
- 755 25. Klemba, A.; Bodnar, L.; Was, H.; Brodaczewska, K. K.; Wcislo, G.; Szczylak, C. A.; Kieda, C., Hypoxia-
756 Mediated Decrease of Ovarian Cancer Cells Reaction to Treatment: Significance for Chemo- and Immunotherapies.
757 *International Journal of Molecular Sciences* **2020**, *21* (24), 9492.
- 758 26. Riffle, S.; Hegde, R. S., Modeling tumor cell adaptations to hypoxia in multicellular tumor spheroids. *Journal of*
759 *Experimental & Clinical Cancer Research* **2017**, *36* (1), 102.
- 760 27. Riffle, S.; Pandey, R. N.; Albert, M.; Hegde, R. S., Linking hypoxia, DNA damage and proliferation in
761 multicellular tumor spheroids. *BMC Cancer* **2017**, *17* (1), 338.
- 762 28. Popova, A. A.; Tronser, T.; Demir, K.; Haitz, P.; Kuodyte, K.; Starkuviene, V.; Wajda, P.; Levkin, P. A., Facile
763 One Step Formation and Screening of Tumor Spheroids Using Droplet-Microarray Platform. *Small* **2019**, *15* (25),
764 1901299.
- 765 29. Däster, S.; Amatruda, N.; Calabrese, D.; Ivanek, R.; Turrini, E.; Droseler, R. A.; Zajac, P.; Fimognari, C.;
766 Spagnoli, G. C.; Iezzi, G.; Mele, V.; Muraro, M. G., Induction of hypoxia and necrosis in multicellular tumor spheroids
767 is associated with resistance to chemotherapy treatment. *Oncotarget* **2016**, *8* (1), 1725-1736.
- 768 30. Stevenson, R. P.; Veltman, D.; Machesky, L. M., Actin-bundling proteins in cancer progression at a glance.
769 *Journal of Cell Science* **2012**, *125* (5), 1073-1079.
- 770 31. Olson, M. F.; Sahai, E., The actin cytoskeleton in cancer cell motility. *Clinical & Experimental Metastasis* **2009**,
771 *26* (4), 273-287.
- 772 32. Klementieva, N. V.; Snopova, L. B.; Prodanets, N. N.; Furman, O. E.; Dudenkova, V. V.; Zagaynova, E. V.;
773 Lukyanov, K. A.; Mishin, A. S., Fluorescence Imaging of Actin Fine Structure in Tumor Tissues Using SiR-Actin Staining.
774 *Anticancer Research* **2016**, *36* (10), 5287-5294.
- 775 33. Baker, A. F.; Malm, S. W.; Pandey, R.; Laughren, C.; Cui, H.; Roe, D.; Chambers, S. K., Evaluation of a
776 hypoxia regulated gene panel in ovarian cancer. *Cancer Microenviron* **2015**, *8* (1), 45-56.
- 777 34. Oguri, S.; Sakakibara, T.; Mase, H.; Shimizu, T.; Ishikawa, K.; Kimura, K.; Smyth, R. D., Clinical
778 pharmacokinetics of carboplatin. *The Journal of Clinical Pharmacology* **1988**, *28* (3), 208-215.
- 779 35. Kessous, R.; Wissing, M. D.; Piedimonte, S.; Abitbol, J.; Kogan, L.; Laskov, I.; Yasmeen, A.; Salvador, S.;
780 Lau, S.; Gotlieb, W. H., CA-125 reduction during neoadjuvant chemotherapy is associated with success of cytoreductive
781 surgery and outcome of patients with advanced high-grade ovarian cancer. *Acta Obstetricia et Gynecologica*
782 *Scandinavica* **2020**, *99* (7), 933-940.
- 783 36. Stage, T. B.; Bergmann, T. K.; Kroetz, D. L., Clinical Pharmacokinetics of Paclitaxel Monotherapy: An Updated
784 Literature Review. *Clinical Pharmacokinetics* **2018**, *57* (1), 7-19.
- 785 37. Zhang, M.; Chen, Z.; Wang, Y.; Zhao, H.; Du, Y., The Role of Cancer-Associated Fibroblasts in Ovarian
786 Cancer. *Cancers (Basel)* **2022**, *14* (11), 2637.
- 787 38. Lou, X.; Zhang, D.; Ling, H.; He, Z.; Sun, J.; Sun, M.; Liu, D., Pure redox-sensitive paclitaxel-maleimide
788 prodrug nanoparticles: Endogenous albumin-induced size switching and improved antitumor efficiency. *Acta*
789 *Pharmaceutica Sinica B* **2021**, *11* (7), 2048-2058.
- 790 39. Li, R.; Zhang, D.; Ren, B.; Cao, S.; Zhou, L.; Xiong, Y.; Sun, Q.; Ren, X., Therapeutic effect of haploididentical
791 peripheral blood stem cell treatment on relapsed/refractory ovarian cancer. *Bulletin du Cancer* **2023**, *110* (3), 285-292.

- 792 40. Lee, J. S.; Kim, S. H.; Lee, S.; Kang, J. H.; Lee, S. H.; Cheong, J. H.; Kim, S. Y., Gastric cancer depends on
793 aldehyde dehydrogenase 3A1 for fatty acid oxidation. *Scientific Reports* **2019**, 9 (1), 16313.
794 41. Kerslake, R.; Belay, B.; Panfilov, S.; Hall, M.; Kyrou, I.; Randeva, H. S.; Hyttinen, J.; Karteris, E.; Sisu, C.,
795 Transcriptional Landscape of 3D vs. 2D Ovarian Cancer Cell Models. *Cancers* **2023**, 15 (13), 3350.
796 42. Hu, Z.; Artibani, M.; Alsaadi, A.; Wietek, N.; Morotti, M.; Shi, T.; Zhong, Z.; Santana Gonzalez, L.; El-
797 Sahhar, S.; KaraminejadRanjbar, M.; Mallett, G.; Feng, Y.; Masuda, K.; Zheng, Y.; Chong, K.; Damato, S.; Dhar,
798 S.; Campo, L.; Garruto Campanile, R.; Soleymani majd, H.; Rai, V.; Maldonado-Perez, D.; Jones, S.; Cerundolo,
799 V.; Sauka-Spengler, T.; Yau, C.; Ahmed, A. A., The Repertoire of Serous Ovarian Cancer Non-genetic Heterogeneity
800 Revealed by Single-Cell Sequencing of Normal Fallopian Tube Epithelial Cells. *Cancer Cell* **2020**, 37 (2), 226-242.e7.
801 43. Ince, T. A.; Sousa, A. D.; Jones, M. A.; Harrell, J. C.; Agoston, E. S.; Krohn, M.; Selfors, L. M.; Liu, W.;
802 Chen, K.; Yong, M.; Buchwald, P.; Wang, B.; Hale, K. S.; Cohick, E.; Sergent, P.; Witt, A.; Kozhekbaeva, Z.; Gao,
803 S.; Agoston, A. T.; Merritt, M. A.; Foster, R.; Rueda, B. R.; Crum, C. P.; Brugge, J. S.; Mills, G. B., Characterization
804 of twenty-five ovarian tumour cell lines that phenocopy primary tumours. *Nature Communications* **2015**, 6, 7419.
805 44. Kopper, O.; de Witte, C. J.; Lohmussaar, K.; Valle-Inclan, J. E.; Hami, N.; Kester, L.; Balgobind, A. V.;
806 Korving, J.; Proost, N.; Begthel, H.; van Wijk, L. M.; Revilla, S. A.; Theeuwesen, R.; van de Ven, M.; van Roosmalen,
807 M. J.; Ponsioen, B.; Ho, V. W. H.; Neel, B. G.; Bosse, T.; Gaarenstroom, K. N.; Vrieling, H.; Vreeswijk, M. P. G.;
808 van Diest, P. J.; Witteveen, P. O.; Jonges, T.; Bos, J. L.; van Oudenaarden, A.; Zweemer, R. P.; Snippert, H. J. G.;
809 Kloosterman, W. P.; Clevers, H., An organoid platform for ovarian cancer captures intra- and interpatient heterogeneity.
810 *Nature Medicine* **2019**, 25 (5), 838-849.
811 45. Inglis, S.; Stewart, S., Metabolic therapeutics in angina pectoris: history revisited with perhexiline. *European
812 Journal of Cardiovascular Nursing* **2006**, 5 (2), 175-184.
813 46. Pettersen, I. K. N.; Tusubira, D.; Ashrafi, H.; Dyrstad, S. E.; Hansen, L.; Liu, X. Z.; Nilsson, L. I. H.; Lovsletten,
814 N. G.; Berge, K.; Wergedahl, H.; Bjorndal, B.; Fluge, O.; Bruland, O.; Rustan, A. C.; Halberg, N.; Rosland, G. V.;
815 Berge, R. K.; Tronstad, K. J., Upregulated PDK4 expression is a sensitive marker of increased fatty acid oxidation.
816 *Mitochondrion* **2019**, 49, 97-110.
817 47. van Weverwijk, A.; Koundouros, N.; Iravani, M.; Ashenden, M.; Gao, Q.; Poulogiannis, G.; Jungwirth, U.;
818 Isacke, C. M., Metabolic adaptability in metastatic breast cancer by AKR1B10-dependent balancing of glycolysis and
819 fatty acid oxidation. *Nature Communications* **2019**, 10 (1), 2698.
820 48. Badmann, S.; Mayr, D.; Schmoekel, E.; Hester, A.; Buschmann, C.; Beyer, S.; Kolben, T.; Kraus, F.;
821 Chelariu-Raicu, A.; Burges, A.; Mahner, S.; Jeschke, U.; Trillsch, F.; Czogalla, B., AKR1C1/2 inhibition by MPA
822 sensitizes platinum resistant ovarian cancer towards carboplatin. *Scientific Reports* **2022**, 12 (1), 1862.
823 49. UK, C. R., Ovarian cancer survival statistics.
824 50. UK, C. R., Cancer survival statistics for all cancers combined.
825 51. Ferreira, L. P.; Gaspar, V. M.; Mano, J. F., Design of spherically structured 3D in vitro tumor models -Advances
826 and prospects. *Acta Biomaterialia* **2018**, 75, 11-34.
827 52. Wadman, M., FDA no longer has to require animal testing for new drugs. *Science* **2023**, 379 (6628), 127-128.
828 53. Seyhan, A. A., Lost in translation: the valley of death across preclinical and clinical divide – identification of
829 problems and overcoming obstacles. *Translational Medicine Communications* **2019**, 4 (1), 18.
830 54. Kola, I.; Landis, J., Can the pharmaceutical industry reduce attrition rates? *Nature Reviews Drug Discovery*
831 **2004**, 3 (8), 711-716.
832 55. Marine, J. C.; Dawson, S. J.; Dawson, M. A., Non-genetic mechanisms of therapeutic resistance in cancer.
833 *Nature Reviews Cancer* **2020**, 20 (12), 743-756.
834 56. Hu, Z.; Cunnea, P.; Zhong, Z.; Lu, H.; Osagie, O. I.; Campo, L.; Artibani, M.; Nixon, K.; Ploski, J.; Santana
835 Gonzalez, L.; Alsaadi, A.; Wietek, N.; Damato, S.; Dhar, S.; Blagden, S. P.; Yau, C.; Hester, J.; Albukhari, A.;
836 Aboagye, E. O.; Fotopoulos, C.; Ahmed, A., The Oxford Classic Links Epithelial-to-Mesenchymal Transition to
837 Immunosuppression in Poor Prognosis Ovarian Cancers. *Clinical Cancer Research* **2021**, 27 (5), 1570-1579.
838 57. Veninga, V.; Voest, E. E., Tumor organoids: Opportunities and challenges to guide precision medicine. *Cancer
839 Cell* **2021**, 39 (9), 1190-1201.
840 58. Even-Ram, S.; Yamada, K. M., Cell migration in 3D matrix. *Current Opinion in Cell Biology* **2005**, 17 (5), 524-
841 532.
842 59. Sodek, K. L.; Ringuette, M. J.; Brown, T. J., Compact spheroid formation by ovarian cancer cells is associated
843 with contractile behavior and an invasive phenotype. *International Journal of Cancer* **2009**, 124 (9), 2060-2070.
844 60. Anderle, N.; Koch, A.; Gierke, B.; Keller, A.-L.; Staebler, A.; Hartkopf, A.; Brucker, S. Y.; Pawlak, M.;
845 Schenke-Layland, K.; Schmees, C., A Platform of Patient-Derived Microtumors Identifies Individual Treatment
846 Responses and Therapeutic Vulnerabilities in Ovarian Cancer. *Cancers* **2022**, 14 (12), 2895.
847 61. Motohara, T.; Masuda, K.; Morotti, M.; Zheng, Y.; El-Sahhar, S.; Chong, K. Y.; Wietek, N.; Alsaadi, A.;
848 Karaminejadranjbar, M.; Hu, Z.; Artibani, M.; Gonzalez, L. S.; Kataabuchi, H.; Saya, H.; Ahmed, A. A., An evolving
849 story of the metastatic voyage of ovarian cancer cells: cellular and molecular orchestration of the adipose-rich metastatic
850 microenvironment. *Oncogene* **2019**, 38 (16), 2885-2898.
851 62. Nowicka, A.; Marini, F. C.; Solley, T. N.; Elizondo, P. B.; Zhang, Y.; Sharp, H. J.; Broaddus, R.; Kolonin,
852 M.; Mok, S. C.; Thompson, M. S.; Woodward, W. A.; Lu, K.; Salimian, B.; Nagrath, D.; Klopp, A. H., Human omental-

- 853 derived adipose stem cells increase ovarian cancer proliferation, migration, and chemoresistance. *PLoS One* **2013**, 8
854 (12), e81859.
855 63. Penning, T. M.; Jonnalagadda, S.; Trippier, P. C.; Rizner, T. L., Aldo-Keto Reductases and Cancer Drug
856 Resistance. *Pharmacological Reviews* **2021**, 73 (3), 1150-1171.
857 64. Freyre, C. A. C.; Rauher, P. C.; Ejsing, C. S.; Klemm, R. W., MIGA2 Links Mitochondria, the ER, and Lipid
858 Droplets and Promotes De Novo Lipogenesis in Adipocytes. *Mol Cell* **2019**, 76 (5), 811-825 e14.
859 65. Ma, S.; Mukherjee, N.; Mikhailova, E.; Bayley, H., Gel Microrods for 3D Tissue Printing. *Advanced Biosystems*
860 **2017**, 1 (8), 1700075.
861
862